Stepwise activation mechanism of the scramblase nhTMEM16 revealed by cryo-EM

Valeria Kalienkova[1], Vanessa Clerico Mosina[2], Laura Bryner[1], Gert T. Oostergetel[2], Raimund Dutzler[1,3*] and Cristina Paulino[2,3,4*]

[1]Department of Biochemistry University of Zürich, Winterthurer Str. 190, CH-8057 Zürich, Switzerland

[2]Department of Structural Biology at the Groningen Biomolecular Sciences and Biotechnology Institute, University of Groningen, Nijenborgh 7, 9747 AG Groningen, The Netherlands

[3]Senior author

[4]Lead contact

[*]Correspondence: dutzler@bioc.uzh.ch (R.D.), c.paulino@rug.nl (C.P.)

SUMMARY

Scramblases catalyze the movement of lipids between both leaflets of a bilayer. Whereas the X-ray structure of the protein nhTMEM16 has previously revealed the architecture of a Ca^{2+}-dependent lipid scramblase, its regulation mechanism has remained elusive. Here, we have used cryo-electron microscopy and functional assays to address this question. Ligand-bound and ligand-free conformations of nhTMEM16 in detergents and lipid nanodiscs illustrate the interactions with its environment and they reveal the conformational changes underlying its activation. In this process, Ca^{2+}-binding induces a stepwise transition of the catalytic subunit cavity, converting a closed cavity that is shielded from the membrane in the absence of ligand, into a polar furrow that becomes accessible to lipid headgroups in the ligand-bound state. Additionally, our structures demonstrate how nhTMEM16 distorts the membrane at both entrances of the subunit cavity, thereby decreasing the energy barrier for lipid movement.

Keywords:

TMEM16 family, lipid scramblase, membrane protein structure, transport mechanism, cryo-EM, single particle

INTRODUCTION

The movement of lipids between both leaflets of a phospholipid bilayer, which is also referred to as lipid flip-flop, is energetically unfavorable since it requires the transfer of the polar headgroup from its aqueous environment across the hydrophobic core of the membrane (Kornberg and McConnell, 1971). Consequently, spontaneous lipid flip-flop is rare and occurs at a time scale of several hours. Whereas the sparsity of this event permits the maintenance of lipid asymmetry, there are processes that require the rapid transbilayer movement of lipids (Bevers and Williamson, 2016; Sanyal and Menon, 2009). Proteins that facilitate this movement, by lowering the associated high energy barrier, are termed lipid scramblases (Pomorski and Menon, 2006; Williamson, 2015). Lipid scramblases are generally non-selective and do not require the input of energy. They participate in various cellular functions ranging from lipid signaling during blood coagulation and apoptosis, to the synthesis of membranes, cell division and exocytosis (Nagata et al., 2016; Whitlock and Hartzell, 2016). First structural insight into lipid scrambling was provided by the X-ray structure of the fungal protein nhTMEM16 (Brunner et al., 2014). This protein is part of the TMEM16 family (Milenkovic et al., 2010), which encompasses calcium-activated ion channels and lipid scramblases with a conserved molecular architecture (Brunner et al., 2016; Caputo et al., 2008; Falzone et al., 2018; Schroeder et al., 2008; Suzuki et al., 2013; Suzuki et al., 2010; Yang et al., 2008). As common for the family, nhTMEM16 is a homodimer with subunits containing a cytoplasmic domain and a transmembrane unit composed of 10 membrane-spanning segments. The lipid permeation path is defined by a structural entity termed the 'subunit cavity', which is located at the periphery of each subunit. In the X-ray structure, which was obtained in the presence of Ca^{2+}, this site exposes a continuous polar cavity that spans the entire membrane and that is of appropriate size to harbor a lipid headgroup (Brunner et al., 2014). The 'subunit cavity' is believed to provide a pathway for the polar moieties of lipids across the membrane, whereas the apolar acyl chains remain embedded in the hydrophobic core of the membrane (Bethel and Grabe, 2016; Brunner et al., 2014; Jiang et al., 2017; Lee et al., 2018; Malvezzi et al., 2018; Stansfeld et al., 2015). This process resembles the credit-card mechanism for lipid scrambling, which was previously proposed based on theoretical considerations (Pomorski and Menon, 2006). Although in this structure, Ca^{2+} ions were identified to bind to a conserved site in the transmembrane domain, the mechanism of how Ca^{2+} activates the protein and how the protein interacts with the surrounding lipids remained elusive. To gain insight into these questions, we have determined structures of the

protein in Ca^{2+}-bound and Ca^{2+}-free conformations by single particle cryo-electron microscopy (cryo-EM), both in detergent and in a membrane environment and we have characterized the effect of mutations on the activation process. Our data reveal two essential features of nhTMEM16. They show how the protein distorts the membrane to lower the energy barrier for lipid movement by steering translocating lipids into the subunit cavity. Additionally, they define the conformational changes leading to the opening of the cavity, which is shielded from the membrane in a Ca^{2+}-free conformation, but exposes a hydrophilic furrow for the permeation of lipids upon Ca^{2+} binding in a stepwise process, involving coupled ligand-dependent and ligand-independent steps.

Results

Structural characterization of nhTMEM16 in detergent

For our investigations of the ligand-induced activation mechanism of the lipid scramblase nhTMEM16, we have recombinantly expressed the protein in the yeast *S. cerevisiae*, purified it in the absence of Ca^{2+} and added the ligand during sample preparation for structure determination and transport experiments. For the structural characterization of nhTMEM16, we have initially studied ligand-bound and ligand-free samples in detergent by cryo-EM. By this approach we have obtained two datasets of high quality and of sufficient resolution (*i.e.* 3.6 Å for Ca^{2+}-bound and 4.0 Å for Ca^{2+}-free conditions) for a detailed interpretation by an atomic model (Figures 1, S1 and S2, Table S1 and Movies S1 and S2). In the data obtained in the presence of Ca^{2+}, we find a conformation of the protein, which closely resembles the X-ray structure with a root mean square deviation (RMSD) of Cα atoms of 0.65 Å (Figures 1A and 1B). The high similarity prevails irrespective of the absence of crystal packing interactions and despite the fact that the sample used for cryo-EM was only briefly exposed to Ca^{2+} at a comparably low (*i.e.* 300 μM) concentration, whereas for the X-ray structure, the protein was exposed to Ca^{2+} during purification and crystallization at a 10-fold higher concentration (Brunner et al., 2014). Cryo-EM density at the conserved Ca^{2+}-binding site, contained within each subunit of the homodimer, clearly indicates the presence of two bound Ca^{2+} ions located at the position originally identified in the X-ray structure (Figure 1C) (Brunner et al., 2014). The structural similarity between cryo-EM and X-ray structures emphasizes that the observed conformation likely displays an active state of the protein rather than an inactive state caused by prolonged exposure to Ca^{2+}. Remarkably, we found a very

similar structure of the protein in the absence of Ca^{2+}, thus underlining the stability of this conformation in detergent solution irrespective of the presence of the ligand (Figures 1D and 1E). Although both structures display equivalent conformations of the protein, the structure determined in the absence of Ca^{2+} clearly shows an altered distribution of the ligand in its binding site, concomitantly with a weaker density of the C-terminal part of α6, which hints at a larger mobility of this helix in the absence of Ca^{2+} (Figure 1D, 1F, S2G and S2H). In this structure, both strong peaks of the ligand found in the Ca^{2+}-bound conformation are absent and instead replaced by a weak residual density at low contour located between the two Ca^{2+} positions (Figure 1F). Since, due to the presence of mM amounts of EGTA, the free Ca^{2+}-concentration is estimated to be in the low nM range, this density might either correspond to a bound water molecule or a Na^{+} ion, which is present in the sample buffer at a concentration of 150 mM. We think that the observed stability of the subunit cavity displayed in structures in detergent, irrespectively of the presence of ligand, does not reflect an intrinsic property of the protein but instead might be a consequence of experimental conditions, which stabilize the observed conformation. The Ca^{2+}-free conformation in detergent might thus display a conformation that is responsible for the basal activity of nhTMEM16 and other fungal scramblases observed in scrambling experiments (Figure S3A) (Brunner et al., 2014; Malvezzi et al., 2013).

Structure of the Ca^{2+}-bound and Ca^{2+}-free states of nhTMEM16 in lipid nanodiscs

The absence of ligand-induced conformational transitions of nhTMEM16 in detergent motivated us to study the structure of the protein in a lipid bilayer. For that purpose, we have reconstituted nhTMEM16 into nanodiscs of different sizes using a lipid composition at which the protein retains its activity as lipid scramblase, although with significantly slower kinetics (Figures S3A and S3B). These samples were used to determine structures of ligand-bound and ligand-free states in a native-like environment at a resolution of 3.6 Å and 3.8 Å, respectively (Figures 2, S3 to S5, Table S1, and Movies S3 and S4). In all cases, the protein is located close to the center of an oval-shaped disc with its long dimensions oriented about parallel to the short diameter, a behavior that is more pronounced at high lipid to protein ratio resulting in larger discs (Figures S3C to S3E). The orientation reflects a preference of lipids for locations distant from the subunit cavity, which appears to destabilize the bilayer. In the condition used for data collection at high resolution, nanodiscs were assembled with 2N2 scaffolding protein at a lipid to protein ratio of 145:1, which

results in assemblies that are approximately 165 x 140 Å in size (Figure S3C). Datasets in both conditions are of excellent quality and provide an unambiguous view of nhTMEM16 in different conformations (Figures 2, S4 and S5, and Table S1).

The differences between structures of nhTMEM16 determined in detergents and in a lipid environment are most pronounced for the Ca^{2+}-free state (Figures 2A and 2B). Whereas the structure in detergent displays a conformation where the subunit cavity is accessible to the membrane, the same region has changed its accessibility in the nanodisc sample. Here, the movement of α4 has led to a collapse of the cavity, similar to a conformation observed in the ion channel TMEM16A (Figures 2B and 2C). This movement is accompanied by a conformational change of α6, as a consequence of the absence of stabilizing interactions with the ligands (Figures 2B and 2D). Generally, the Ca^{2+}-free state of nhTMEM16 in nanodiscs is very similar to the equivalent structure of the lipid scramblase TMEM16F, which is described in an accompanying paper, thus underlining that both structures display an inactive conformation of the scramblase in the absence of ligand (Figure S6A). Different from the data of the Ca^{2+}-free protein in nanodiscs, the cryo-EM data obtained for the Ca^{2+}-bound samples in nanodiscs shows a large conformational heterogeneity along the subunit cavity, as reflected in the weaker densities for α-helices 3 and 4 (Figures 2E and S5). The predominant conformation shows well-resolved cryo-EM densities for two Ca^{2+} ions and a rigid structure of α6, in place coordinating the ligand (Figure 2E and 2H). Compared to the ligand-free structure in nanodiscs, the positions of α-helices 3 and 4 have changed, leading to a conformation with a widened subunit cavity (Figures 2F, S6B and S6C). This conformation thus displays an intermediate between the closed Ca^{2+}-free state determined in nanodiscs and the fully open Ca^{2+}-bound conformation observed in detergent (Figures 2F, 2G, S6B and S6C). When subjected to a final 3D classification, besides the described predominant conformation two minor populations could be identified, with one conformation resembling the ligand-bound open state obtained in detergent and another the closed conformation obtained in lipid nanodiscs in absence of ligand (Figure S5). The distinct distribution of states, with a majority of nhTMEM16 residing in a potentially inactive conformation, is reflected in the lower activity of the protein in this lipid composition (Figure S3A) and it emphasizes the equilibrium between intermediate and open conformations in the Ca^{2+}-bound state.

Conformational transitions

The diversity of conformations of nhTMEM16 observed in various datasets and the presence of different populations in the Ca^{2+}-bound sample in lipid nanodiscs, suggest that our structures represent distinct states of a stepwise activation process. In all structures, the core of the protein is conserved and the largest movements are observed in the vicinity of the subunit cavity (Figures 2B, 2F, 2G and 3, and Movie S5). The Ca^{2+}-bound conformation in detergents, which closely resembles the X-ray structure, shows the widest opening of the subunit cavity and thus likely depicts a scrambling-competent state of the protein (Figure 3A). In this presumably 'open state', α-helices 4 and 6 are separated from each other on their entire length framing the two opposite edges of a semicircular polar cavity that is exposed to the lipid bilayer (Figure 3A). In this case, the interaction of α3 with α10 of the adjacent subunit on the intracellular side appears to limit the movement of the tightly interacting α4, thus preventing a further widening of the cavity on the intracellular side (Figures 4A and 4B). On the opposite border of the cavity, α6 is immobilized in its position by the bound Ca^{2+} ions, which results in a tight interaction with α7 and α8 (Figure s 4B and 4C). In the main class of the nanodisc sample in the presence of ligand, we find marked conformational changes compared to the 'open state' of the detergent structure. The most pronounced differences are found for the α3-α4 pair (Figure 4). The intracellular part of α3 (but not the α2-α3 loop contacting the helix Cα1 following α10) has detached from its interaction with α10, leading to a concomitant movement of α4 at the same region (Figure 4A). This movement has also affected the conformation of the extracellular part of α4, which has approached α6 thereby forming initial contacts between both helices (Figures 3B and 4B). The subunit cavity in this conformation is no longer exposed to the membrane at its extracellular part and the structure thus likely represents an intermediate of the scramblase towards activation (Figure 3B). This 'intermediate state' is remarkable in light of the observed ion conduction in nhTMEM16 and other TMEM16 scramblases (see accompanying manuscript) (Lee et al., 2016; Suzuki et al., 2013; Yang et al., 2012; Yu et al., 2015), as it displays a conformation containing a potential protein-enclosed aqueous pore (Figures S6B and S6C). The interactions between α4 and α6 tighten in the Ca^{2+}-free conformation observed in nanodiscs, thereby constricting the aqueous pore observed in the 'intermediate state' (Figures 3C, 4B, 4C, S6B and S6C). Here, the dissociation of the ligand from the protein has allowed a relaxation of α6 leading to its detachment from α8 at the intracellular part of the helix (Figures 4B and 4C). Although, unlike TMEM16A and TMEM16F, nhTMEM16

does not contain a flexible glycine residue at the hinge, the movements occur at a similar region (Paulino et al., 2017a). The observed changes at its intracellular part are accompanied by comparatively smaller rearrangements of α6 extracellular to the binding site (Figures 3C, 4B and 4C). These rearrangements likely promote a further reorientation of the extracellular half of α4 towards α6 and a tightening of the interaction interface between both α-helices, resulting in a conformation that resembles equivalent interactions in the ion channel TMEM16A and the lipid scramblase TMEM16F (Figures 2C, 3C, 4B and S6A, see also accompanying manuscript). In the transition from an 'open' to a 'closed state' α4 undergoes the largest changes among all parts of nhTMEM16 with two prolines (Pro 332 and Pro 341) and a glycine (Gly 339) serving as potential pivots for helix-rearrangements (Figure 4D). Remarkably, both prolines are conserved among fungal homologues and Pro 332 is also found in TMEM16K, the closest mammalian orthologue of nhTMEM16.

Protein-induced distortion of the lipid environment

A remarkable feature observed in the cryo-EM maps concerns the arrangement of detergent or lipid molecules surrounding nhTMEM16, which allowed us to characterize the influence of the protein on its environment. Neither detergent molecules nor nanodisc lipids are uniformly distributed on the outside of nhTMEM16. Instead, they adapt to the shape of the protein with distortions observed in the vicinity of the shorter α-helices 1 and 8 at the extracellular side and at the gap between α-helices 4 and 6 at the intracellular side. The observed distortions are found to a similar extent in all determined structures, irrespective of the presence or absence of calcium ions in detergent or lipid nanodiscs and can thus be considered as a state-independent property of the protein. These distortions result in a marked deviation from the annular shape of detergents or surrounding lipids found in most membrane proteins (Figure 5 and Movie S6). Remarkably, the resulting undulated distribution contains depressions in both, the detergent or lipid density close to the entrances of the subunit cavity. The arrangement of the protein with its long dimension parallel to the short diameter of the oval-shaped nanodiscs reflects the preferential location of lipids at sites away from the subunit cavity (Figure S3C to S3D). The protein affects the distribution of lipids and the shape of the plane of the bilayer in nanodiscs, which is slightly V-shaped and locally deviates from planarity at several regions (Figure 5B). These pronounced depressions thin and distort the lipid structure at both ends of the subunit cavity, thereby likely

facilitating the entry of polar head-groups into the cavity and lowering the barrier for lipid movement (Figure 5C).

Functional properties of mutants affecting the activation process

The distinct conformations of nhTMEM16 determined in this study hint at a sequential mechanism, in which Ca^{2+}-dependent and independent steps are coupled to promote activation similar to ligand-dependent channels. We have thus investigated the functional consequences of mutations of residues of the ligand-binding site and of the moving parts of α4. For that purpose, we have purified point mutants, reconstituted them into liposomes containing fluorescently labeled lipids and characterized lipid transport using an assay that follows the irreversible decay of the fluorescence upon addition of the membrane-impermeable reducing agent dithionite to the outside of the liposomes (Brunner et al., 2014; Malvezzi et al., 2013; Ploier and Menon, 2016). The mutation D503A located on α7 concerns a residue of the Ca^{2+} binding site that does not change its structure in different protein conformations and thus clearly affects the initial ligand-binding step (Figure 6A). In this case, we find a Ca^{2+}-dependent scrambling activity although with strongly decreased potency of the ligand (Figures 6B and 6C). Next, we investigated whether the mutation of two proline residues and a close-by glycine (Pro 332, Gly 339 and Pro 341), which form potential pivots during the rearrangement of α4 would alter lipid scrambling (Figure 6A). Whereas we did not find a pronounced effect in the mutant P341A, the mutants G339A and P332A showed a strongly decreased activity both, in the presence and absence of Ca^{2+} (but no obvious change in the Ca^{2+}-potency of the protein, Figures 6D to 6F and S7). As these residues do not face the subunit cavity in the 'open state' we assume that these mutants alter the equilibrium between active and inactive conformations, thus emphasizing the role of conformational changes in α-helix 4 for activation.

Discussion

By combining data from cryo-electron microscopy and biochemical assays, our study has addressed two important open questions concerning the function of a TMEM16 scramblase: It has revealed the conformational changes that lead to the activation of nhTMEM16 in response to ligand binding and it has shown how the protein interacts with the surrounding membrane to facilitate lipid translocation. Structures in ligand-free and bound states reveal distinct

conformations of nhTMEM16, which capture the catalytic subunit cavity of the scramblase at different levels of exposure to the membrane during the activation process, representing a 'closed', 'intermediate' and 'open' states (Figure 3 and Movie S5). As different protein conformations are observed in presence and absence of its ligand, we propose a stepwise activation mechanism for TMEM16 scramblases, where all states are at equilibrium (Figure 7). Here, the Ca^{2+}-free conformation obtained in nanodiscs defines a non-conductive state of the protein, where the polar subunit cavity has collapsed and is shielded from the membrane by tight interactions of α4 and α6 on the extracellular part of the membrane (Figures 2A and 3C). The protein surface of the closed subunit cavity is hydrophobic as expected for a membrane protein. This 'closed state' of nhTMEM16 resembles equivalent structures obtained for the lipid scramblase TMEM16F (as described in an accompanying manuscript) and the ion channel TMEM16A (Figures 2C and S6A) (Dang et al., 2017; Paulino et al., 2017a; Paulino et al., 2017b), thus underlining that it is representative for an inactive conformation of both functional branches of the family. In this conformation, the Ca^{2+}-binding site is empty, with the intracellular part of α6 positioned apart from the remainder of the binding site to release the electrostatic strain induced by the large negative net-charge in this region. The high mobility of this region is reflected in its weak cryo-EM density (Figures 2A, 2D, S4G and S4H). Details of the conformational change of α6 differ between the three family members of known structure with the conformation in nhTMEM16 being closer to the one observed for TMEM16F (Figure S6A and accompanying manuscript) (Paulino et al., 2017a). During the activation process, Ca^{2+} binding provides interactions with residues on α6. The helix rearranges into a locked state, as manifested in the well resolved cryo-EM density for its intracellular half, which shields the binding site from the cytoplasm (Figures 1A, 2E, S1G, S1H, S5G and S5H). This Ca^{2+}-induced movement of α6 in nhTMEM16 is coupled to rearrangements in its interface with α4, thereby weakening the interactions and resulting in a widening of the cavity (Figures 2F, 3B, 4B, 4C, S6B and S6C). This partially-opened cavity is defined by the main population observed in the Ca^{2+}-bound nhTMEM16 structure in nanodiscs (Figures 2E and 3B). As the subunit cavity is not yet exposed to the membrane, this conformation likely does not promote lipid scrambling. Instead, it might have opened a protein-enclosed pore that could facilitate the observed ion conduction, which has been described as by-product of lipid scrambling in nhTMEM16 (Lee et al., 2016), and which is a hallmark of the lipid scramblase TMEM16F (Yang et al., 2012; Yu et al., 2015) (see accompanying manuscript). Following the initial Ca^{2+}-

induced conformational transition, the activation of lipid scrambling requires a second step, which leads to a larger reorientation of α-helices 3 and 4 and a subsequent opening of the polar subunit cavity to the membrane (Figures 2B, 3A, 4, S6B and S6C). This open state is defined by the Ca^{2+}-bound structure of nhTMEM16 obtained in detergent and by one of the subclasses observed in the nanodisc dataset (Figures 1A and S5D). Thus, ion conduction and lipid-scrambling in nhTMEM16 and other TMEM16 scramblases might be mediated by distinct conformations which are at equilibrium in a Ca^{2+}-bound protein (Figure 7). This stepwise activation mechanism is in general accordance with molecular dynamics simulations, which have started from the fully Ca^{2+}-bound open structure and for which transitions leading to a partial closure of the subunit cavity have been observed in the trajectories (Jiang et al., 2017; Lee et al., 2018). The basal scrambling activity of nhTMEM16 is likely a consequence of the equilibrium between open, intermediate and closed conformations, which is strongly shifted towards the closed state in the absence of Ca^{2+}. This is consistent with the observation of a Ca^{2+}-free open state in detergent but not in nanodiscs, where the detergent environment favors the equilibrium towards the open conformation (Figures 1D to 1F).

The cryo-EM structures of nhTMEM16 also reveal how the protein interacts with the surrounding membrane to disturb its structure and consequently lower the energy barrier for lipid flip-flop, as predicted from molecular dynamics simulations (Bethel and Grabe, 2016; Jiang et al., 2017; Lee et al., 2018; Stansfeld et al., 2015). Our data reveal a pronounced distortion of the protein-surrounding environment, which is stronger than observed for the ion channel TMEM16A (Paulino et al., 2017b). This effect is preserved in all four datasets, irrespectively of the presence or absence of ligand in detergent or nanodiscs, as their underlying structural features change little in the different conformations. The distortion causes a deviation of the detergent or lipid molecules surrounding nhTMEM16 from the annular structure observed in most membrane proteins (Figure 5 and Movie S6). The resulting bent of the membrane in vicinity of both entrances of the subunit cavity serves to channel lipids into the catalytic unit on their way across the membrane.

In summary, our structures of nhTMEM16 have described how a calcium-activated lipid scramblase is activated in a stepwise manner and how it bends the membrane to promote the transport of lipids between both leaflets of the membrane by a mechanism that is likely conserved within the family.

SUPPLEMENTAL INFORMATION

Supplemental Information includes seven figures, one table and six movies and can be found with this article online at:

ACKNOWLEDGMENTS

We thank S. Klauser, S. Rast and M. Punter for their help in establishing and maintaining the computer infrastructure, H. Stahlberg and K. Goldie at C-Cina (University of Basel, Switzerland) for access to cryo-electron microscopes at an initial stage of the project. D. Deneka is acknowledged for his advice on lipid nanodisc reconstitution. All members of the Dutzler and Paulino labs are acknowledged for help at various stages of the project. This work was supported by a grant from the European Research Council (no 339116, AnoBest) to R.D. and by a grant from the NWO Start-Up (no 740.018.016) to C.P..

AUTHOR CONTRIBUTIONS

V.K. and L.B. purified proteins for cryo-EM and functional characterization. V.K. reconstituted protein into nanodiscs and liposomes and carried out lipid transport experiments. V.K. and C.P. prepared the samples for cryo-EM. V.K., V.C.M., G.T.O. and C.P. collected cryo-EM data. V.K., V.C.M and C.P. carried out image processing, model building and refinement. V.K., V.C.M, R.D. and C.P. jointly planned experiments, analyzed the data and wrote the manuscript.

DECLARATION OF INTERESTS

The authors have no financial interests to declare.

REFERENCES

Adams, P.D., Afonine, P.V., Bunkoczi, G., Chen, V.B., Davis, I.W., Echols, N., Headd, J.J., Hung, L.W., Kapral, G.J., Grosse-Kunstleve, R.W.*, et al.* (2010). PHENIX: a comprehensive Python-based system for macromolecular structure solution. Acta Crystallogr. D Biol. Crystallogr. *66*, 213-221.

Bers, D.M., Patton, C.W., and Nuccitelli, R. (2010). A practical guide to the preparation of Ca(2+) buffers. Method. Cell Biol. *99*, 1-26.

Bethel, N.P., and Grabe, M. (2016). Atomistic insight into lipid translocation by a TMEM16 scramblase. Proc. Natl. Acad. Sci. USA *113*, 14049-14054.

Bevers, E.M., and Williamson, P.L. (2016). Getting to the Outer Leaflet: Physiology of Phosphatidylserine Exposure at the Plasma Membrane. Physiol. Rev. *96*, 605-645.

Biyani, N., Righetto, R.D., McLeod, R., Caujolle-Bert, D., Castano-Diez, D., Goldie, K.N., and Stahlberg, H. (2017). Focus: The interface between data collection and data processing in cryo-EM. J. Struct. Biol. *198*, 124-133.

Brunner, J.D., Lim, N.K., Schenck, S., Duerst, A., and Dutzler, R. (2014). X-ray structure of a calcium-activated TMEM16 lipid scramblase. Nature *516*, 207-212.

Brunner, J.D., Schenck, S., and Dutzler, R. (2016). Structural basis for phospholipid scrambling in the TMEM16 family. Curr. Opin. Struct. Biol. *39*, 61-70.

Caputo, A., Caci, E., Ferrera, L., Pedemonte, N., Barsanti, C., Sondo, E., Pfeffer, U., Ravazzolo, R., Zegarra-Moran, O., and Galietta, L.J. (2008). TMEM16A, a membrane protein associated with calcium-dependent chloride channel activity. Science *322*, 590-594.

Chen, S., McMullan, G., Faruqi, A.R., Murshudov, G.N., Short, J.M., Scheres, S.H., and Henderson, R. (2013). High-resolution noise substitution to measure overfitting and validate resolution in 3D structure determination by single particle electron cryomicroscopy. Ultramicroscopy *135*, 24-35.

Dang, S., Feng, S., Tien, J., Peters, C.J., Bulkley, D., Lolicato, M., Zhao, J., Zuberbuhler, K., Ye, W., Qi, L.*, et al.* (2017). Cryo-EM structures of the TMEM16A calcium-activated chloride channel. Nature *552*, 426-429.

Emsley, P., and Cowtan, K. (2004). Coot: model-building tools for molecular graphics. Acta Crystallogr. D Biol. Crystallogr. *60*, 2126-2132.

Falzone, M.E., Malvezzi, M., Lee, B.C., and Accardi, A. (2018). Known structures and unknown mechanisms of TMEM16 scramblases and channels. J. Gen. Physiol. *150*, 933-947.

Geertsma, E.R., and Dutzler, R. (2011). A versatile and efficient high-throughput cloning tool for structural biology. Biochemistry *50*, 3272-3278.

Gietz, R.D., and Schiestl, R.H. (2007). High-efficiency yeast transformation using the LiAc/SS carrier DNA/PEG method. Nat. Protoc. *2*, 31-34.

Goddard, T.D., Huang, C.C., Meng, E.C., Pettersen, E.F., Couch, G.S., Morris, J.H., and Ferrin, T.E. (2018). UCSF ChimeraX: Meeting modern challenges in visualization and analysis. Protein Sci. *27*, 14-25.

Jiang, T., Yu, K., Hartzell, H.C., and Tajkhorshid, E. (2017). Lipids and ions traverse the membrane by the same physical pathway in the nhTMEM16 scramblase. eLife *6*, e28671.

Kimanius, D., Forsberg, B.O., Scheres, S.H., and Lindahl, E. (2016). Accelerated cryo-EM structure determination with parallelisation using GPUs in RELION-2. eLife *5*, e18722.

Kornberg, R.D., and McConnell, H.M. (1971). Inside-outside transitions of phospholipids in vesicle membranes. Biochemistry *10*, 1111-1120.

Lee, B.C., Khelashvili, G., Falzone, M., Menon, A.K., Weinstein, H., and Accardi, A. (2018). Gating mechanism of the extracellular entry to the lipid pathway in a TMEM16 scramblase. Nat. Commun. *9*, 3251.

Lee, B.C., Menon, A.K., and Accardi, A. (2016). The nhTMEM16 Scramblase Is Also a Nonselective Ion Channel. Biophys. J. *111*, 1919-1924.

Malvezzi, M., Andra, K.K., Pandey, K., Lee, B.C., Falzone, M.E., Brown, A., Iqbal, R., Menon, A.K., and Accardi, A. (2018). Out-of-the-groove transport of lipids by TMEM16 and GPCR scramblases. Proc. Natl. Acad. Sci. USA *115*, 7033-7042.

Malvezzi, M., Chalat, M., Janjusevic, R., Picollo, A., Terashima, H., Menon, A.K., and Accardi, A. (2013). Ca2+-dependent phospholipid scrambling by a reconstituted TMEM16 ion channel. Nat. Commun. *4*, 2367.

Milenkovic, V.M., Brockmann, M., Stohr, H., Weber, B.H., and Strauss, O. (2010). Evolution and functional divergence of the anoctamin family of membrane proteins. BMC Evol. Biol. *10*, 319.

Nagata, S., Suzuki, J., Segawa, K., and Fujii, T. (2016). Exposure of phosphatidylserine on the cell surface. Cell Death Differ. *23*, 952-961.

Paulino, C., Kalienkova, V., Lam, A.K.M., Neldner, Y., and Dutzler, R. (2017a). Activation mechanism of the calcium-activated chloride channel TMEM16A revealed by cryo-EM. Nature *552*, 421-425.

Paulino, C., Neldner, Y., Lam, A.K., Kalienkova, V., Brunner, J.D., Schenck, S., and Dutzler, R. (2017b). Structural basis for anion conduction in the calcium-activated chloride channel TMEM16A. eLife *6*, e26232.

Pettersen, E.F., Goddard, T.D., Huang, C.C., Couch, G.S., Greenblatt, D.M., Meng, E.C., and Ferrin, T.E. (2004). UCSF Chimera – a visualization system for exploratory research and analysis. J. Comput. Chem. *25*, 1605-1612.

Ploier, B., and Menon, A.K. (2016). A Fluorescence-based Assay of Phospholipid Scramblase Activity. J. Vis. Exp. *115*.

Pomorski, T., and Menon, A.K. (2006). Lipid flippases and their biological functions. Cell Mol. Life Sci. *63*, 2908-2921.

Ritchie, T.K., Grinkova, Y.V., Bayburt, T.H., Denisov, I.G., Zolnerciks, J.K., Atkins, W.M., and Sligar, S.G. (2009). Chapter 11 – Reconstitution of membrane proteins in phospholipid bilayer nanodiscs. Method. Enzymol. *464*, 211-231.

Rohou, A., and Grigorieff, N. (2015). CTFFIND4: Fast and accurate defocus estimation from electron micrographs. J. Struct. Biol. *192*, 216-221.

Rosenthal, P.B., and Henderson, R. (2003). Optimal determination of particle orientation, absolute hand, and contrast loss in single-particle electron cryomicroscopy. J. Mol. Biol. *333*, 721-745.

Sanyal, S., and Menon, A.K. (2009). Flipping lipids: why an' what's the reason for? ACS Chem. Biol. *4*, 895-909.

Scheres, S.H., and Chen, S. (2012). Prevention of overfitting in cryo-EM structure determination. Nat. Methods *9*, 853-854.

Schroeder, B.C., Cheng, T., Jan, Y.N., and Jan, L.Y. (2008). Expression cloning of TMEM16A as a calcium-activated chloride channel subunit. Cell *134*, 1019-1029.

Smart, O.S., Neduvelil, J.G., Wang, X., Wallace, B.A., and Sansom, M.S. (1996). HOLE: a program for the analysis of the pore dimensions of ion channel structural models. J. Mol. Graph. *14*, 354-360, 376.

Stansfeld, P.J., Goose, J.E., Caffrey, M., Carpenter, E.P., Parker, J.L., Newstead, S., and Sansom, M.S. (2015). MemProtMD: Automated Insertion of Membrane Protein Structures into Explicit Lipid Membranes. Structure *23*, 1350-1361.

Suzuki, J., Fujii, T., Imao, T., Ishihara, K., Kuba, H., and Nagata, S. (2013). Calcium-dependent phospholipid scramblase activity of TMEM16 protein family members. J. Biol. Chem. *288*, 13305-13316.

Suzuki, J., Umeda, M., Sims, P.J., and Nagata, S. (2010). Calcium-dependent phospholipid scrambling by TMEM16F. Nature *468*, 834-838.

Tan, Y.Z., Baldwin, P.R., Davis, J.H., Williamson, J.R., Potter, C.S., Carragher, B., and Lyumkis, D. (2017). Addressing preferred specimen orientation in single-particle cryo-EM through tilting. Nat. Methods *14*, 793-796.

Whitlock, J.M., and Hartzell, H.C. (2016). Anoctamins/TMEM16 Proteins: Chloride Channels Flirting with Lipids and Extracellular Vesicles. Annu. Rev. Physiol. *79*, 119-143.

Williamson, P. (2015). Phospholipid Scramblases. Lipid Insights *8*, 41-44.

Yang, H., Kim, A., David, T., Palmer, D., Jin, T., Tien, J., Huang, F., Cheng, T., Coughlin, S.R., Jan, Y.N.*, et al.* (2012). TMEM16F forms a Ca2+-activated cation channel required for lipid scrambling in platelets during blood coagulation. Cell *151*, 111-122.

Yang, Y.D., Cho, H., Koo, J.Y., Tak, M.H., Cho, Y., Shim, W.S., Park, S.P., Lee, J., Lee, B., Kim, B.M.*, et al.* (2008). TMEM16A confers receptor-activated calcium-dependent chloride conductance. Nature *455*, 1210-1215.

Yu, K., Whitlock, J.M., Lee, K., Ortlund, E.A., Cui, Y.Y., and Hartzell, H.C. (2015). Identification of a lipid scrambling domain in ANO6/TMEM16F. eLife *4*, e06901.

Zheng, L., Baumann, U., and Reymond, J.L. (2004). An efficient one-step site-directed and site-saturation mutagenesis protocol. Nucleic Acids Res. *32*, e115.

Zheng, S.Q., Palovcak, E., Armache, J.P., Verba, K.A., Cheng, Y., and Agard, D.A. (2017). MotionCor2: anisotropic correction of beam-induced motion for improved cryo-electron microscopy. Nat. Methods *14*, 331-332.

Zivanov, J., Nakane, T., Forsberg, B., Kimanius, D., Hagen, W.J.H., Lindahl, E., and Scheres, S.H.W. (2018). RELION-3: new tools for automated high-resolution cryo-EM structure determination. bioRxiv.

FIGURES AND FIGURE LEGENDS

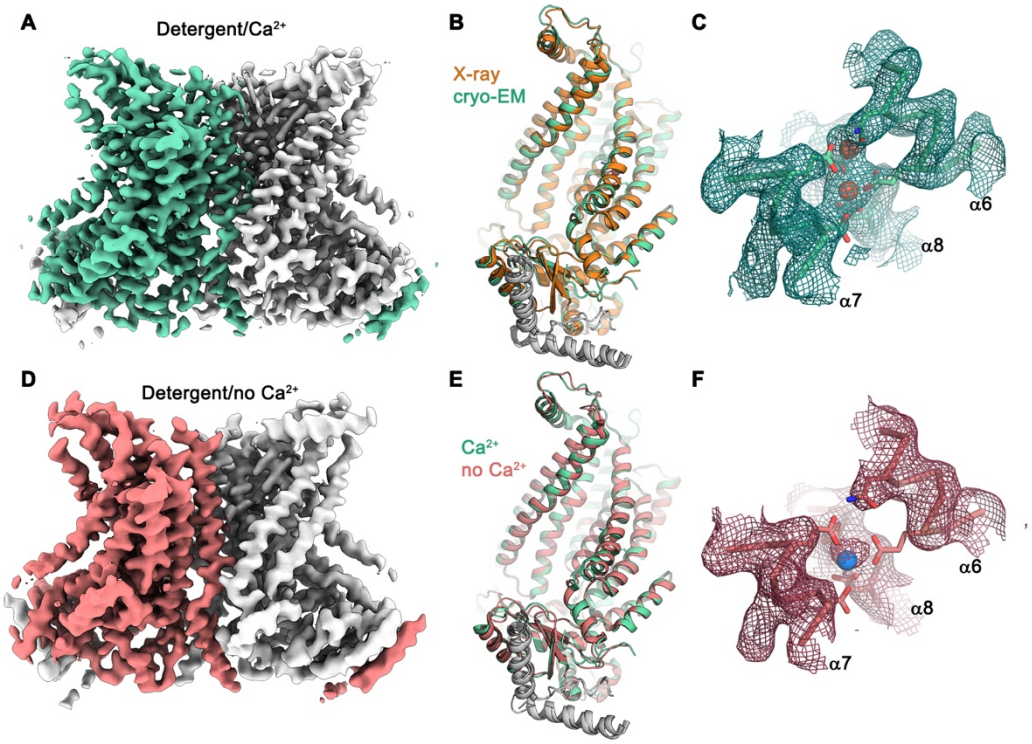

Figure 1. Cryo-EM structures of nhTMEM16 in detergent

(A) Cryo-EM map of the nhTMEM16 dimer (light green and grey) in DDM-β in presence of Ca^{2+} at 3.6 Å sharpened with a b-factor of –126 $Å^2$ and contoured at 6 σ. (B) Ribbon representation of a superposition of the Ca^{2+}-bound structure in detergent determined by cryo-EM (green and grey) and the Ca^{2+}-bound X-ray structure (orange and grey, PDBID: 4WIS). (C) View of the Ca^{2+}-ion binding site of the Ca^{2+}-bound state of nhTMEM16 in DDM-β. Ca^{2+}-ions are displayed as orange spheres. (D) Cryo-EM map of the nhTMEM16 dimer (light red and grey) in DDM-β in the absence of Ca^{2+} at 4.0 Å sharpened with a b-factor of –187 $Å^2$ and contoured at 6 σ. (E) Ribbon representation of a superposition of the Ca^{2+}-bound (light green and grey) and the Ca^{2+}-free structure (light red and grey) in detergent determined by cryo-EM. (F) View of the Ca^{2+}-binding site in the Ca^{2+}-free state of nhTMEM16 in DDM-β. The location of weak residual density at the center of the Ca^{2+}-binding site is indicated by a blue sphere. (C and F), The respective cryo-EM densities are contoured at 6 σ and shown as mesh. The backbone is displayed as Cα-trace, selected side-chains as sticks. See also Figures S1 and S2, Table S1 and Movies S1 and S2.

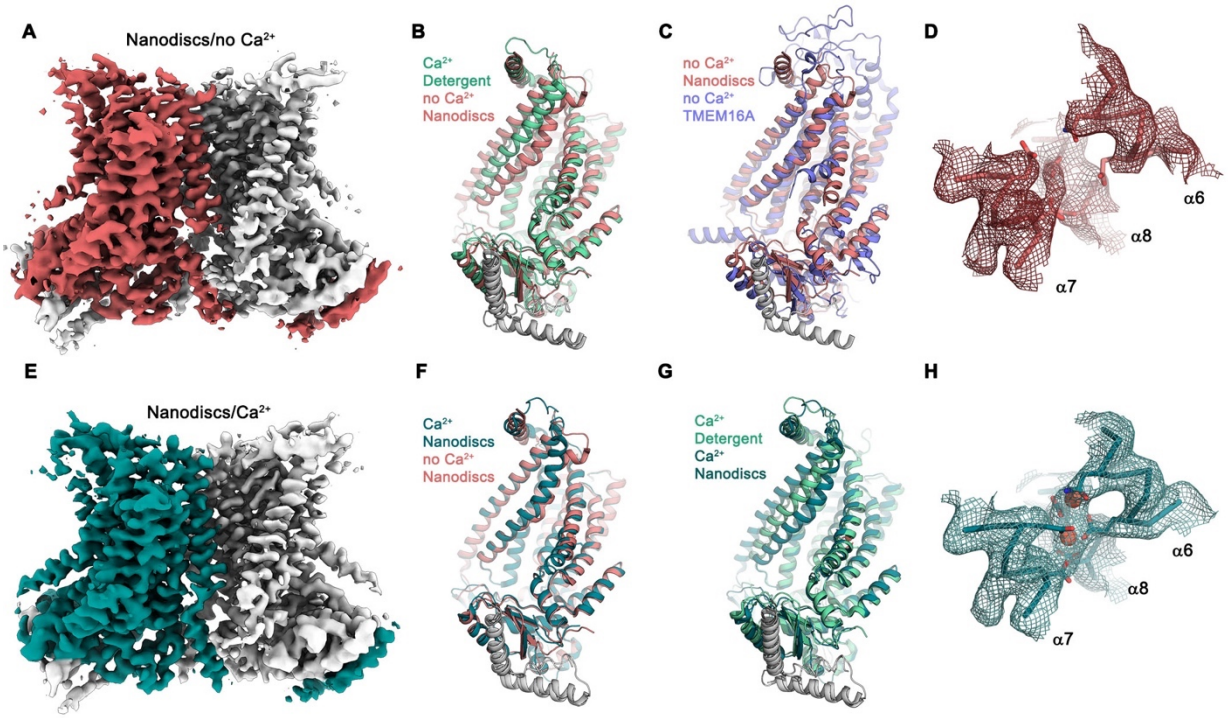

Figure 2. Cryo-EM structures of nhTMEM16 in nanodiscs

(A) Cryo-EM map of the nhTMEM16 dimer (dark red and grey) in nanodiscs in absence of Ca^{2+} at 3.8 Å sharpened with a b-factor of –150 $Å^2$ and contoured at 4.8 σ. (B and C) Ribbon representation of superpositions of the Ca^{2+}-free structure in nanodiscs (dark red and grey) and the Ca^{2+}-bound structure in DDM-β (B, light green and grey) and the Ca^{2+}-free structure of TMEM16A (C, violet, PDBID: 5OYG). (D) View of the Ca^{2+}-binding site in the Ca^{2+}-free state of nhTMEM16 in nanodiscs. (E) Cryo-EM map of the nhTMEM16 dimer (dark green and grey) in nanodiscs in the presence of Ca^{2+} at 3.6 Å sharpened with a b-factor of –157 $Å^2$ and contoured at 5.4 σ. (F and G) Ribbon representation of a superposition of Ca^{2+}-bound structure of nhTMEM16 in nanodiscs (dark green and grey) and the Ca^{2+}-free structure in nanodiscs (F, dark red and grey) and the Ca^{2+}-bound structure in DDM-β (G, light green and grey). (H) View of the Ca^{2+}-binding site in the Ca^{2+}-bound state of nhTMEM16 in nanodiscs. Ca^{2+}-ions are displayed as orange spheres. (D and H) The respective cryo-EM densities contoured at 6 σ are shown as mesh, the backbone is displayed as Cα-trace, selected side-chains as sticks. See also Figures S3, S4 and S5, Table S1 and Movies S3 and S4.

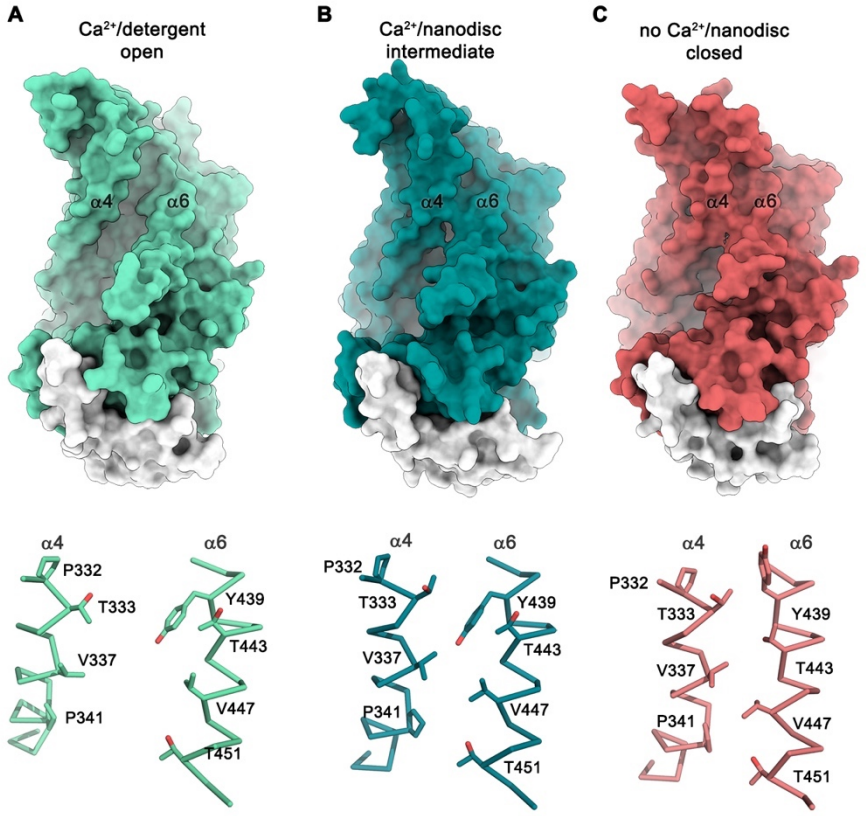

Figure 3. States of the 'subunit cavity'

(A to C) View of the molecular surface of the subunit cavity (top) and structure of the interacting regions of α4 and α6 displayed as Cα-trace with selected sidechains shown as sticks and labeled (bottom). (A) 'Open state' as defined in the Ca^{2+}-bound structure in detergent. (B) 'Intermediate state' as defined by the Ca^{2+}-bound structure in nanodiscs. (C) 'Closed state' as defined by the Ca^{2+}-free structure in nanodiscs. See also Figure S6 and Movie S5.

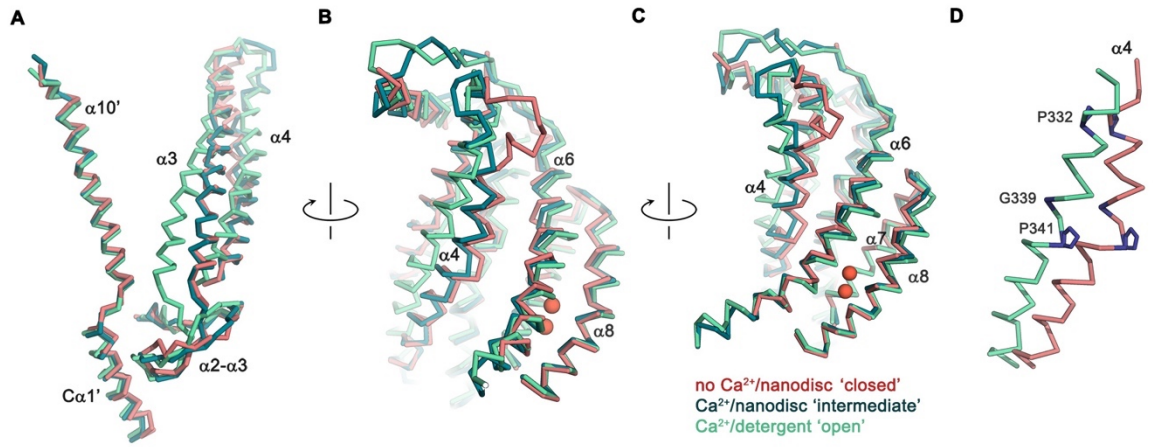

Figure 4. Conformational changes

(A to C) Cα-traces of selected regions of the 'subunit cavity' in different conformations. The relationship between views is indicated and Ca^{2+} ions are shown as orange spheres. (D) Superposition of α4 in the 'open' and closed' states with residues that act as potential pivots for structural arrangements highlighted in blue. See also Figure S6.

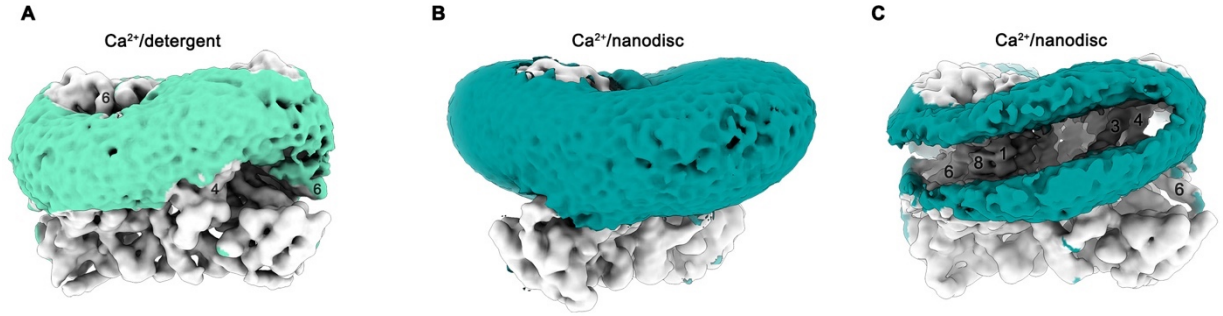

Figure 5. Detergent and lipid interactions

(A) Unmasked cryo-EM density map of the Ca^{2+}-bound nhTMEM16 data in detergent contoured at 4 σ. The detergent belt is colored in light green. (B and C) Unmasked cryo-EM density map of the Ca^{2+}-bound nhTMEM16 data in lipid nanodiscs. The lipid region is colored in dark green. (B), Map contoured at 4 σ displaying the boundaries of the nanodiscs. (C) Clipped map contoured at 4σ indicating the headgroup regions of both membrane leaflets. (A to C) The view is from within the membrane; selected α-helices are indicated. See also Movie S6.

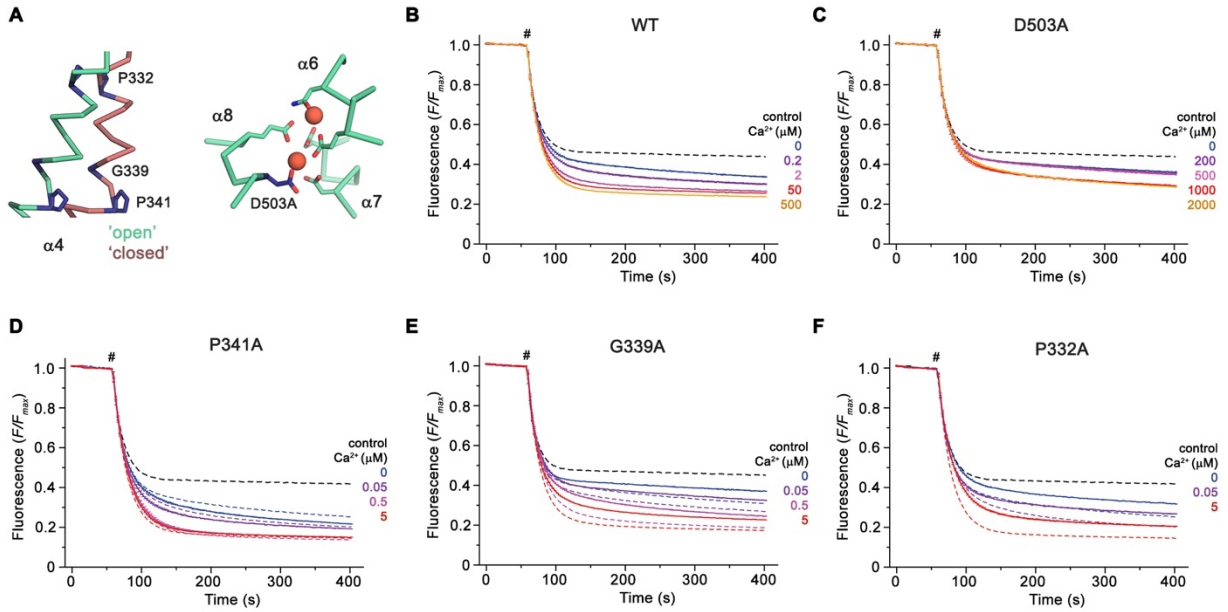

Figure 6. Functional properties of mutants

(A) Regions of nhTMEM16 harboring mutated residues. Left, Cα-trace of α4 in 'open' and 'closed' conformations. Right, ion binding site with Ca^{2+}-ions shown in orange. (B to F) Ca^{2+}-dependence of scrambling activity in nhTMEM16-containing proteoliposomes. Traces depict fluorescence decrease of tail-labeled NBD-PE lipids after addition of dithionite (#) at different Ca^{2+} concentrations. Data show averages of three technical replicates. Ca^{2+} concentrations (μM) are indicated. (B) WT, (C) D503A, (D) P341A, (E) G339A, and (F) P332A. (D to F) The traces of WT reconstituted in the same batch of liposomes are shown as dashed lines in the same color as their corresponding conditions of the mutant for comparison. (B to F), The black dashed line refers to the fluorescence decay in protein-free liposomes. See also Figure S7.

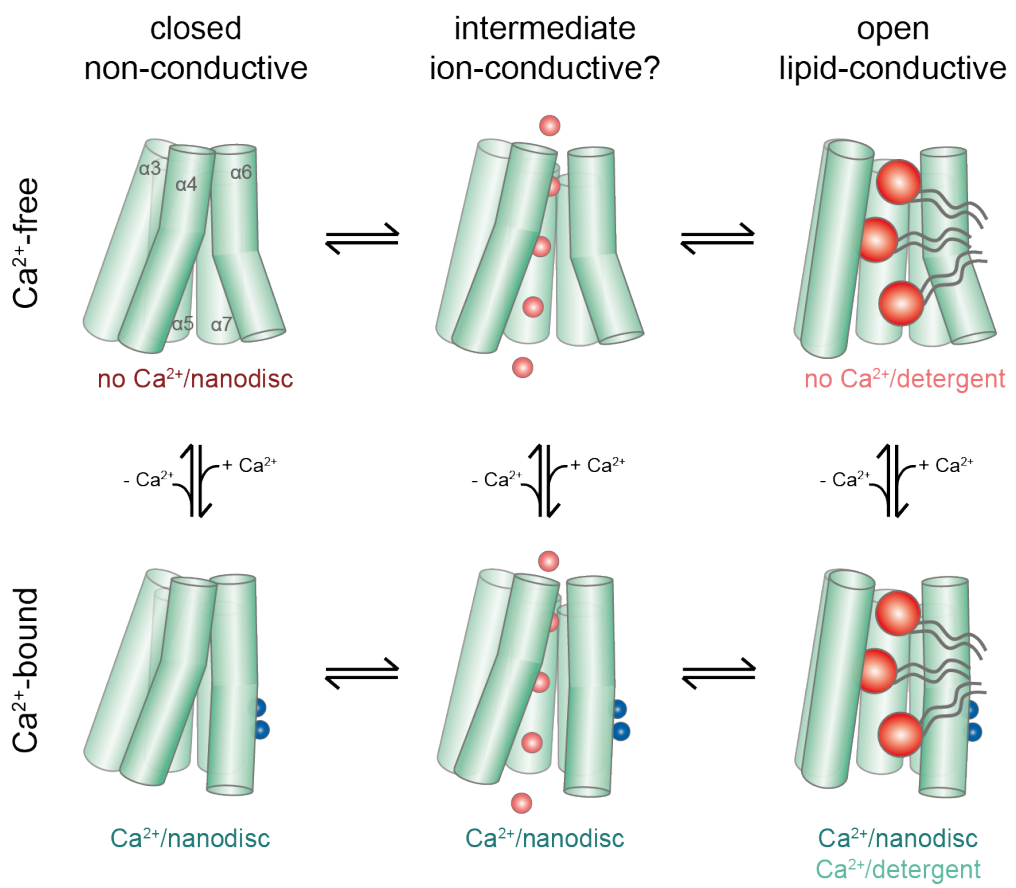

Figure 7. Activation mechanism

Scheme of the stepwise activation of nhTMEM16 displaying the equilibrium of states in Ca^{2+}-bound and Ca^{2+}-free conditions. Conformations obtained in this study and their correspondence to distinct states are indicated. Ca^{2+} and permeating ions are depicted as blue and red spheres, respectively. Phospholipid headgroups are shown as red spheres and acyl chains as grey tails.

METHODS

Contact for Reagent and Resource Sharing

Further information and requests for resources and reagents should be directed to and will be fulfilled by the Lead Contact, Cristina Paulino (c.paulino@rug.nl).

Strains

Wild type *S. cerevisiae* FGY217 were grown either on YPD agar or in YPD liquid media supplemented with 2% glucose at 30 °C. After the transformation with respective plasmids, the cells were grown on yeast synthetic drop-out media without uracil with 2% glucose at 30 °C. For protein expression, the cells were transferred into a selective media containing 0.1% glucose.

Construct preparation

The sequence encoding nhTMEM16 was cloned into a modified FX-cloning compatible (Geertsma and Dutzler, 2011) pYES2 vector as a C-terminal fusion to streptavidin-binding peptide (SBP) and Myc tags that were followed by a HRV 3C cleavage site. The mutations were introduced using a QuickChange method (Zheng et al., 2004).

Protein expression and purification

All buffers were prepared using Ca^{2+}-free water for molecular biology. Plasmids carrying the WT or mutant genes were transformed into the *S. cerevisiae* FGY217 strain as described (Gietz and Schiestl, 2007) using lithium acetate/single-stranded carrier DNA/polyethylene glycol method. The cells carrying the plasmid were grown at 30 °C in a yeast synthetic dropout media until the culture reached the OD_{600} of 0.8. Afterwards, the protein expression was initialized by adding 2% galactose and the temperature was decreased to 25 °C. The protein was expressed for 40 hours after induction. Cells were harvested at 5,500 rpm for 10 min and resuspended in buffer A (50 mM HEPES pH 7.6, 150 mM NaCl, 10 mM EGTA) containing 1 mM $MgCl_2$, DNAse and protease inhibitor cocktail tablets and lysed using a high pressure cell lyser HPL6 at 40 KPsi. Cell-debris

was removed by centrifugation at 8,000 g for 30 min. Membranes were subsequently harvested by centrifugation at 200,000 g for 1.5 hours, resuspended in buffer A containing 5% glycerol and flash-frozen in liquid N_2 and stored at -80 °C until further use. During purification, all steps were carried out at 4 °C or on ice. Membranes were solubilized in buffer A containing 2% *n*-dodecyl-β-d-maltopyranoside (DDM-β) and 5% glycerol for 1.5 h. The insoluble fraction was removed by ultracentrifugation at 42,000 rpm for 30 min. The supernatant was applied to streptavidin Ultralink resin for 1.5 h, incubated under gentle agitation. The resin containing bound protein was subsequently washed with 50 column volumes (CV) of buffer B (10 mM HEPES pH 7.6, 150 mM NaCl, 5 mM EGTA, 0.03% DDM-β, 5% glycerol).

For sample preparation for cryo EM in detergent, the purification tag was cleaved on the resin with HRV 3C protease in buffer B containing 20 μg/ml of yeast polar lipids for 2 h. The flow-through was collected, concentrated using 100 kDa cut-off centrifugal filter units at 700 g and injected into Superdex 200 size-exclusion column equilibrated in buffer C (5 mM HEPES pH 7.6, 150 mM NaCl, 2 mM EGTA, 0.03% DDM-β). Main peak fractions were pooled, yeast polar lipids were added to the sample to a final concentration of 20 μg/ml. Afterwards, the protein was concentrated to 3.3 mg/ml as described above.

For sample preparation in lipid nanodiscs, membrane scaffold protein (MSP) 2N2 was expressed and purified as described (Ritchie et al., 2009), except that the polyhistidine-tag was not removed. Chloroform-solubilized lipids (POPC:POPG at a molar ratio of 7:3) were pooled, dried under a nitrogen stream, and washed twice with diethyl ether. The resulting lipid film was dried in a desiccator overnight, and solubilized in 30 mM DDM-β at a final lipid concentration of 10 mM. nhTMEM16 was purified as described above, except that the uncleaved fusion construct was eluted from the beads with buffer B containing 3 mM biotin. Protein-containing fractions were pooled and concentrated as described above. Biotin was removed from the sample via gelfiltration on a Superdex 200 column. Purified protein was assembled into 2N2 nanodiscs at a molar ratio of protein:lipids:MSP of 2:725:10 as described (Ritchie et al., 2009). Briefly, nhTMEM16 was mixed with detergent-solubilized lipids and incubated on ice for 30 min. Subsequently, purified 2N2 was added to the sample, and the mixture was incubated for additional 30 min. Detergent was removed by incubating of the sample overnight with SM-2 biobeads (200 mg of beads/ml of the reaction) under constant rotation. From this point on, detergent was excluded from all buffers. To separate

the protein-containing from empty nanodiscs, the sample was incubated with streptavidin resin for 1.5 hours. The resin was washed with 3 CV of buffer B and assembled nanodiscs containing nhTMEM16 were eluted in buffer B containing 3 mM biotin. The purification tag was removed by incubation with HRV 3C protease for 2 hours. Cleaved samples were concentrated at 500 *g* using concentrators (Amicon) with a molecular weight cut-off of 100 kDa and injected onto a Superose 6 column equilibrated in buffer C. Analogously to the detergent sample, the main peak fractions were concentrated to around 2 mg/ml.

For reconstitution into proteoliposomes, nhTMEM16 was purified as described for detergent samples used for cryo EM with minor differences: lysate was incubated with streptactin resin and eluted in buffer B containing 5 mM of d-desthiobiotin and the purification tag was not removed.

Reconstitution into the liposomes and scrambling assay

Functional reconstitution was carried out essentially as described (Malvezzi et al., 2013). Lipids for the reconstitution *(E. coli* polar extract and eggPC at a ratio of 3:1 (w/w) supplemented with 0.5% (w/w) 18:1-06:0 NBD-PE) were pooled and dried as described above. The lipid film was dissolved in assay buffer A (20 mM HEPES pH 7.5, 300 mM KCl, 2 mM EGTA) containing 35 mM CHAPS at a final lipid concentration of 20 mg/ml, aliquoted, flash-frozen and stored until further use. On the day of reconstitution, lipids were diluted to 4 mg/ml in assay buffer A and purified protein was added to the lipid mixture at a lipid to protein ratio of 300:1 (w/w). The mixture was incubated for 15 min at room temperature (RT). Biobeads (15 mg of beads/mg of lipids) were added in 4 steps (after 15 min, 30 min, 1 h and 12 h). After the second addition of biobeads, the sample was transferred to 4 °C. The proteoliposomes were harvested by centrifugation (150,000 *g*, 30 min, 4 °C), resuspended in assay buffer A containing desired amounts of free Ca^{2+} (calculated with the WEBMAXC calculator) (Bers et al., 2010) at a final concentration of 10 mg/ml, flash-frozen and stored at -80 °C until further use. On the day of the measurement, the liposomes were frozen and thawed 3 times and extruded through a 400 nm polycarbonate membrane 21 times. Scrambling data was recorded on a Horiba Fluoromax spectrometer. For the measurement, liposomes were diluted to 0.2 mg/ml in assay buffer B (80 mM HEPES pH 7.5, 300 mM KCl, 2 mM EGTA) containing corresponding amounts of free Ca^{2+}.

Sodium dithionite was added after 60 sec to a final concentration of 30 mM and the fluorescence decay was recorded for additional 340 sec. Data were normalized as F/Fmax. Reconstitution efficiency of mutants as compared to wild type nhTMEM16 was estimated by Western blotting using a semi-dry transfer protocol. Protein was detected using mouse anti-c-Myc antibody as a primary (1:5,000 dilution) and goat anti-mouse coupled to a peroxidase as a secondary antibody (1:10,000 dilution).

Cryo-electron microscopy sample preparation and imaging

2.5 µl of freshly purified protein at a concentration of 3.3 mg/ml when solubilized in DDM-β and around 2 mg/ml when reconstituted in nanodiscs were applied on holey-carbon cryo-EM grids (Quantifoil Au R1.2/1.3, 200, 300 and 400 mesh), which were prior glow-discharged at 5 mA for 30 s. For datasets of Ca^{2+}-bound protein, samples (containing 2mM EGTA) were supplemented with 2.3 mM $CaCl_2$ before freezing, resulting in a free calcium concentration of 300 µM. Grids were blotted for 2–5 s in a Vitrobot (Mark IV, Thermo Fisher) at 10– 15 °C and 100% humidity, plunge-frozen in liquid ethane and stored in liquid nitrogen until further use. Cryo-EM data were collected on a 200 keV Talos Arctica microscope (Thermo Fisher) using a post-column energy filter (Gatan) in zero-loss mode, a 20 eV slit, a 100 µm objective aperture, in an automated fashion using EPU software (Thermo Fisher) on a K2 summit detector (Gatan) in counting mode. Cryo-EM images were acquired at a pixel size of 1.012 Å (calibrated magnification of 49,407x), a defocus range from –0.5 to –2 µm, an exposure time of 9 s with a sub-frame exposure time of 150 ms (60 frames), and a total electron exposure on the specimen of about 52 electrons per $Å^2$. The best regions on the grid were screened and selected with an in-house written script to calculate the ice thickness and data quality was monitored on-the-fly using the software FOCUS (Biyani et al., 2017).

Image Processing

For the detergent dataset collected in presence of Ca^{2+}, the 2,521 dose-fractionated cryo-EM images recorded (final pixel size 1.012 Å) were subjected to motion-correction and dose-weighting

of frames by MotionCor2 (Zheng et al., 2017). The CTF parameters were estimated on the movie frames by ctffind4.1 (Rohou and Grigorieff, 2015). Images showing contamination, a defocus above –0.5 or below –2 µm, or a poor CTF estimation were discarded. The resulting 2,023 images were used for further analysis with the software package RELION2.1 (Kimanius et al., 2016). Around 4,000 particles were initially manually picked from a subset of the dataset and classified to create a reference for autopicking. The final round of autopicking on the whole dataset yielded 251,693 particles, which were extracted with a box size of 220 pixels and initial classification steps were performed with two-fold binned data. False positives were removed in the first round of 2D classification. Remaining particles were subjected to several rounds of 2D classification, resulting in 174,901 particles that were further sorted in several rounds of 3D classification. A map created from the X-ray structure of nhTMEM16 (PDBID: 4WIS) was low-pass filtered to 50 Å and used as initial reference for the first round of 3D classification. The resulting best output class was used as new reference in subsequent jobs in an iterative way. The best 3D classes, comprising 128,648 particles, were subjected to auto-refinement, yielding a map with a resolution of 4.3 Å. In the last refinement iteration, a mask excluding the micelle was used and the refinement was continued until convergence, which improved the resolution to 4.0 Å. The final map was masked and sharpened during post-processing resulting in a resolution of 3.9 Å. Finally, the newly available algorithms for CTF refinement and Bayesian polishing implemented in Relion3.0, were applied to further improve the resolution (Zivanov et al., 2018). A last round of 3D classification was performed, resulting in 120,086 particles that were subjected to refinement, providing a mask generated from the final PDB model in the last iteration. The final map at 3.6 Å resolution was sharpened using an isotropic B-factor of -126 $Å^2$. During final 3D classification and auto-refinement, a C2-symmetry was imposed. Local resolution was estimated by RELION. All resolutions were estimated using the 0.143 cut-off criterion (Rosenthal and Henderson, 2003) with gold-standard Fourier shell correlation (FSC) between two independently refined half maps (Scheres and Chen, 2012). During post-processing, the approach of high-resolution noise substitution was used to correct for convolution effects of real-space masking on the FSC curve (Chen et al., 2013). The directional resolution anisotropy of density maps was quantitatively evaluated using 3DFSC (Tan et al., 2017).

For the other datasets, a similar workflow for image processing was applied. In case of the detergent dataset collected in absence of Ca^{2+}, a total of 435,660 particles were extracted with a

box size of 256 pixels from 2,947 images. Several rounds of 2D and 3D classification resulted in a final number of 214,170 particles, which yielded a 4.5 Å map after refinement. After post-processing the resolution improved to 4.0 Å. The dataset in nanodisc in absence of Ca^{2+} resulted in 1,379,187 auto-picked particles from 6,465 images extracted with a box size of 240 pixels, which were reduced to 150,421 particles after several rounds of 2D and 3D classification. CTF refinement and Bayesian polishing followed by a final round of 3D classification was performed, resulting in a selection of 133,961 particles. The final refinement and masking resulted in a 3.8 Å resolution map. Finally, for the dataset in nanodiscs in the presence of Ca^{2+}, 1,379,187 particles were picked from 5,743 images and extracted with a box size of 240 pixels. The final set of 276,232 particles was refined providing a mask in the last iteration, and subsequently post-processed yielding a map at a resolution of 3.6 Å. To assess conformational heterogeneity within the dataset, the nanodiscs was subtracted form the final set of particles and subjected to 3D classification revealing three distinct conformations of the subunit cavity.

Model building refinement and validation

For all datasets, the X-ray structure of nhTMEM16 (PDBID: 4WIS) was used as template. All structures were manually edited in Coot (Emsley and Cowtan, 2004) prior to real-space refinement in Phenix with secondary structure constrains and NCS (Adams et al., 2010). Whereas structures of nhTMEM16 in detergent closely resemble the X-ray structure, pronounced conformational changes for α3 and α4, and to a lesser extent for α6 were observed in structures obtained in lipid nanodiscs. In ambiguous regions, model building was guided by structures refined at higher resolution (i.e. from Ca^{2+}-bound structures of nhTMEM16 in detergent and nanodiscs). For all datasets, it was possible to build the loop connecting the cytoplasmic and the transmembrane domains (residue range 130-140), which was disordered in the X-ray structure. As the loop connecting Cα1-Cα2 was more mobile compared to X-ray structures, residues 651-664 were not modeled. In case of the Ca^{2+}-free structure of nhTMEM16 in nanodiscs, the density of the loop connecting α5' and α6 was weaker than in other structures, and residues 417-424 were not interpreted in this model. For validation of the refinement, Fourier shell correlations (FSC) between the refined model and the final map were determined (FSC_{SUM}, Figures S2E, S3E, S4E

and S5E). To monitor the effects of potential over-fitting, random shifts (up to 0.3 Å) were introduced into the coordinates of the final model, followed by refinement in Phenix against the first unfiltered half-map. The FSC between this shaken-refined model and the first half-map used during validation refinement is termed FSC_{work}, the FSC against the second half-map, which was not used at any point during refinement, FSC_{free}. The marginal gap between the curves describing FSC_{work} and FSC_{free} indicates no over-fitting of the model. Figures were prepared using Pymol (The PyMOL Molecular Graphics System, Version 2.0 Schrödinger, LLC), Chimera (Pettersen et al., 2004) and ChimeraX (Goddard et al., 2018).

SUPPLEMENTAL INFORMATION

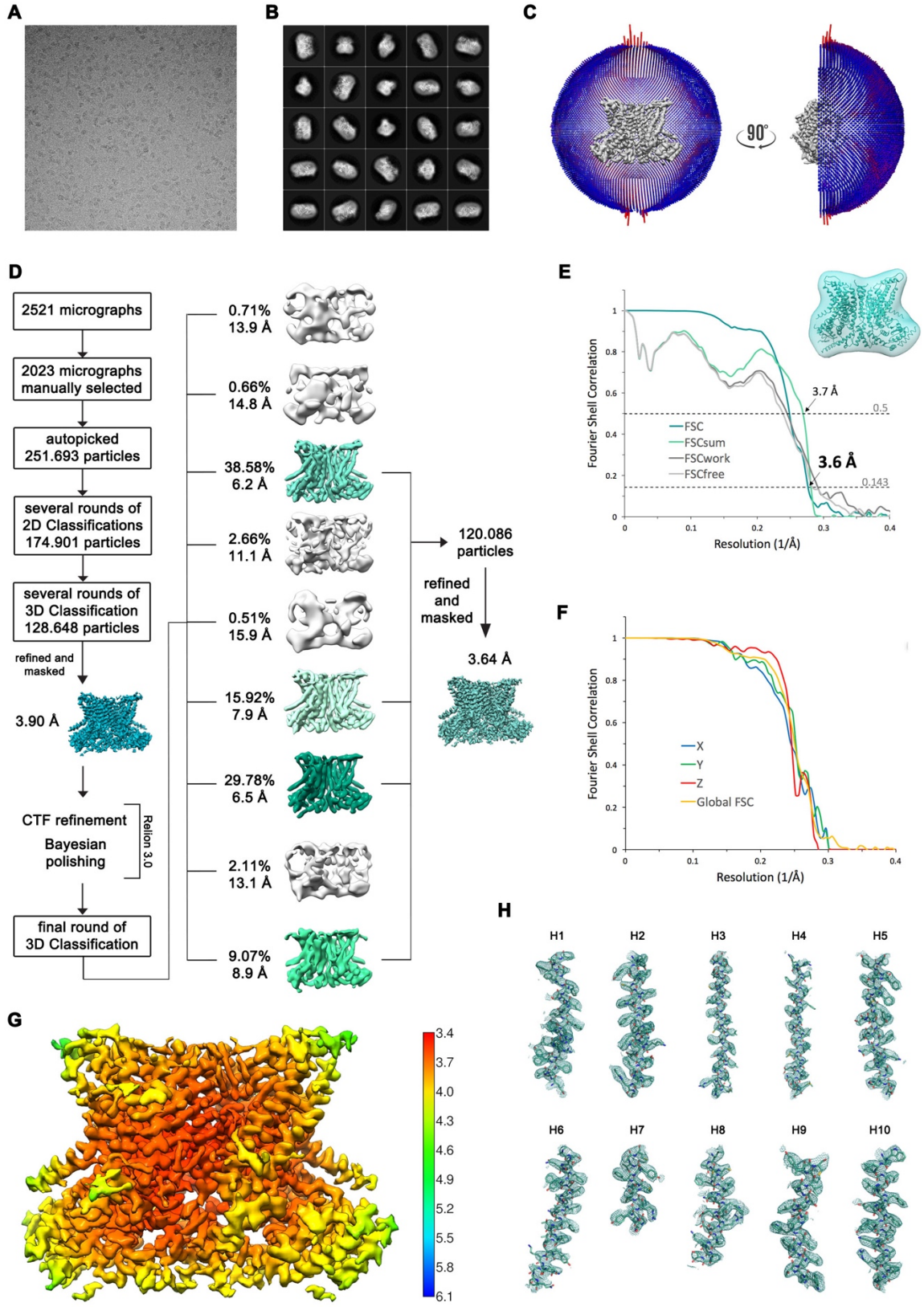

Figure S1. Structure Determination of nhTMEM16 in complex with Ca^{2+} in DDM, Related to Figure 1

(A) Representative cryo- EM image and (B) 2D-class averages of vitrified nhTMEM16 in a Ca^{2+}-bound state in detergent. (C) Angular distribution plot of particles included in the final C2-symmetric 3D reconstruction. The number of particles with their respective orientation is represented by length and color of the cylinders. (D) Image processing workflow. (E) FSC plot used for resolution estimation and model validation. The gold-standard FSC plot between two separately refined half-maps is shown in dark green and indicates a final resolution of 3.6 Å. FSC validation curves for FSCsum, FSCwork and FSCfree as described in Methods are shown in light green, dark grey and light grey, respectively. A thumbnail of the mask used for FSC calculation overlaid on the atomic model is shown in the upper right corner and thresholds used for FSCsum of 0.5 and for FSC, FSCwork and FSCfree of 0.143 are shown as dashed lines. (F) Anisotropy estimation plot of the final map. The global FSC curve is represented in yellow. The directional FSCs along the x, y and z axis displayed in blue, green and red, respectively, are indicative for an isotropic dataset. (G) Final reconstruction map colored by local resolution as estimated by Relion, indicate regions of higher resolution. (H) Sections of the cryo-EM density of the map superimposed on the refined model. The model is shown as sticks and structural elements are labelled. The map was sharpened with a b-factor of –126 $Å^2$ and contoured at 5 σ.

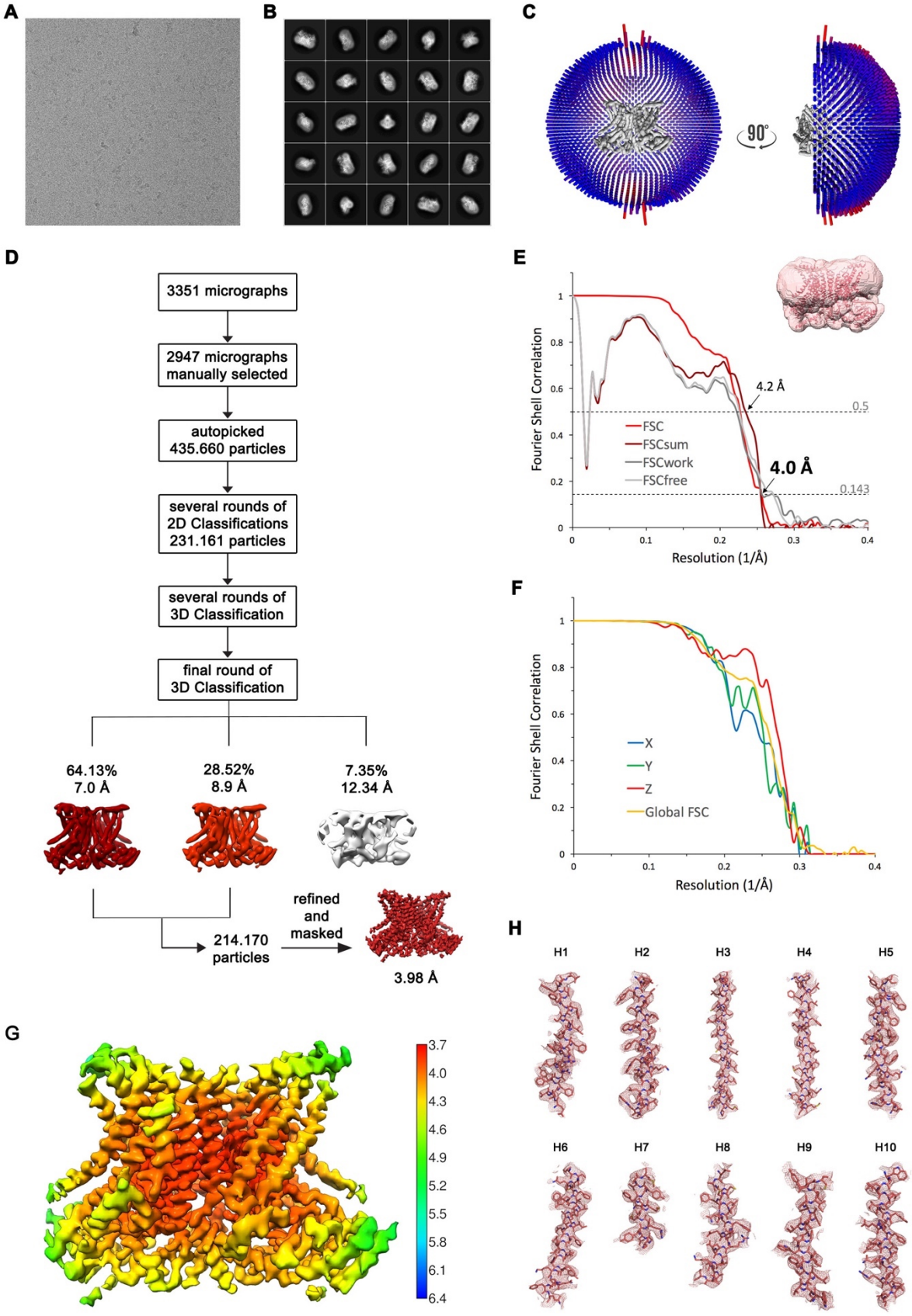
A
B
C
90°
D
3351 micrographs
2947 micrographs manually selected
autopicked 435.660 particles
several rounds of 2D Classifications 231.161 particles
several rounds of 3D Classification
final round of 3D Classification
64.13% 7.0 Å
28.52% 8.9 Å
7.35% 12.34 Å
214.170 particles
refined and masked
3.98 Å
E
Fourier Shell Correlation
Resolution (1/Å)
FSC
FSCsum
FSCwork
FSCfree
4.2 Å
4.0 Å
0.5
0.143
F
Fourier Shell Correlation
Resolution (1/Å)
X
Y
Z
Global FSC
G
3.7
4.0
4.3
4.6
4.9
5.2
5.5
5.8
6.1
6.4
H
H1
H2
H3
H4
H5
H6
H7
H8
H9
H10

Figure S2. Structure Determination of nhTMEM16 in absence of Ca^{2+} in DDM, Related to Figure 1

(A) Representative cryo- EM image and (B) 2D-class averages of vitrified nhTMEM16 in a Ca^{2+}-free state in detergent. (C) Angular distribution plot of particles included in the final C2-symmetric 3D reconstruction. The number of particles with their respective orientation is represented by length and color of the cylinders. (D) Image processing workflow. (E) FSC plot used for resolution estimation and model validation. The gold-standard FSC plot between two separately refined half-maps is shown in red and indicates a final resolution of 4.0 Å. FSC validation curves for FSCsum, FSCwork and FSCfree as described in Methods are shown in dark red, dark grey and light grey, respectively. A thumbnail of the mask used for FSC calculation overlaid on the atomic model is shown in the upper right corner and thresholds used for FSCsum of 0.5 and for FSC, FSCwork and FSCfree of 0.143 are shown as dashed lines. (F) Anisotropy estimation plot of the final map. The global FSC curve is represented in yellow. The directional FSCs along the x, y and z axis displayed in blue, green and red, respectively, are indicative for an isotropic dataset. (G) Final reconstruction map colored by local resolution as estimated by Relion, indicate regions of higher resolution. (H) Sections of the cryo-EM density of the map superimposed on the refined model. The model is shown as sticks and structural elements are labelled. The map was sharpened with a b-factor of –187 $Å^2$ and contoured at 5 σ.

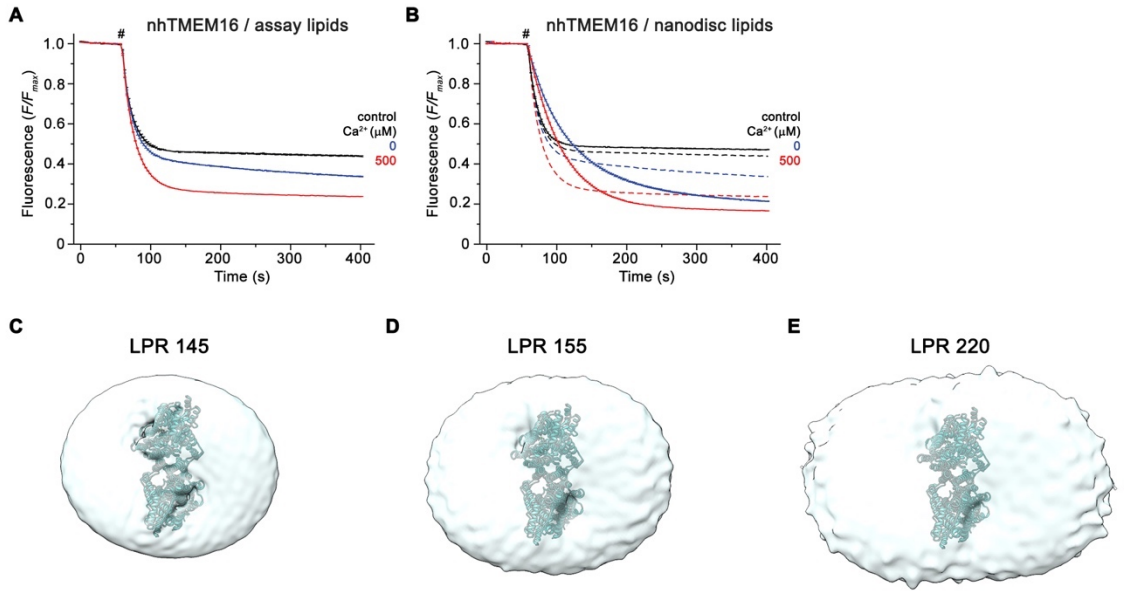

Figure S3. Reconstitution of nhTMEM16 into lipid nanodiscs, Related to Figure 2

(A and B) Ca^{2+}-dependence of scrambling activity of WT in liposomes of two different lipid compositions. Traces depict the fluorescence decrease of tail-labeled NBD-PE lipids after addition of dithionite (#) at different Ca^{2+} concentrations. Data show averages of three technical replicates. Ca^{2+} concentrations (µM) are indicated. (A) Scrambling activity of nhTMEM16 reconstituted into liposomes composed of *E. coli* polar lipids, egg PC at a ratio of 3:1 (w/w) used for functional experiments. (B) Scrambling activity of nhTMEM16 reconstituted into liposomes composed of POPC/POPG at a molar ratio of 7:3 used for nanodisc assembly. Traces of *E. coli* polar lipids/egg PC-containing proteoliposomes (displayed in A) are shown as dashed lines for comparison. (C to D) Geometry of particles of nhTMEM16 reconstituted into nanodiscs at different protein to lipid ratios (LPR) (w/w). Cryo-EM density maps are viewed from the extracellular side. A model of nhTMEM16 fitted into the density is displayed as ribbon. (C) Low-passed filtered map of nhTMEM16 reconstituted at LPR 145. (D) Low resolution cryo-EM density at LPR 155. (E) Low resolution cryo-EM density at LPR 220 (For details see methods).

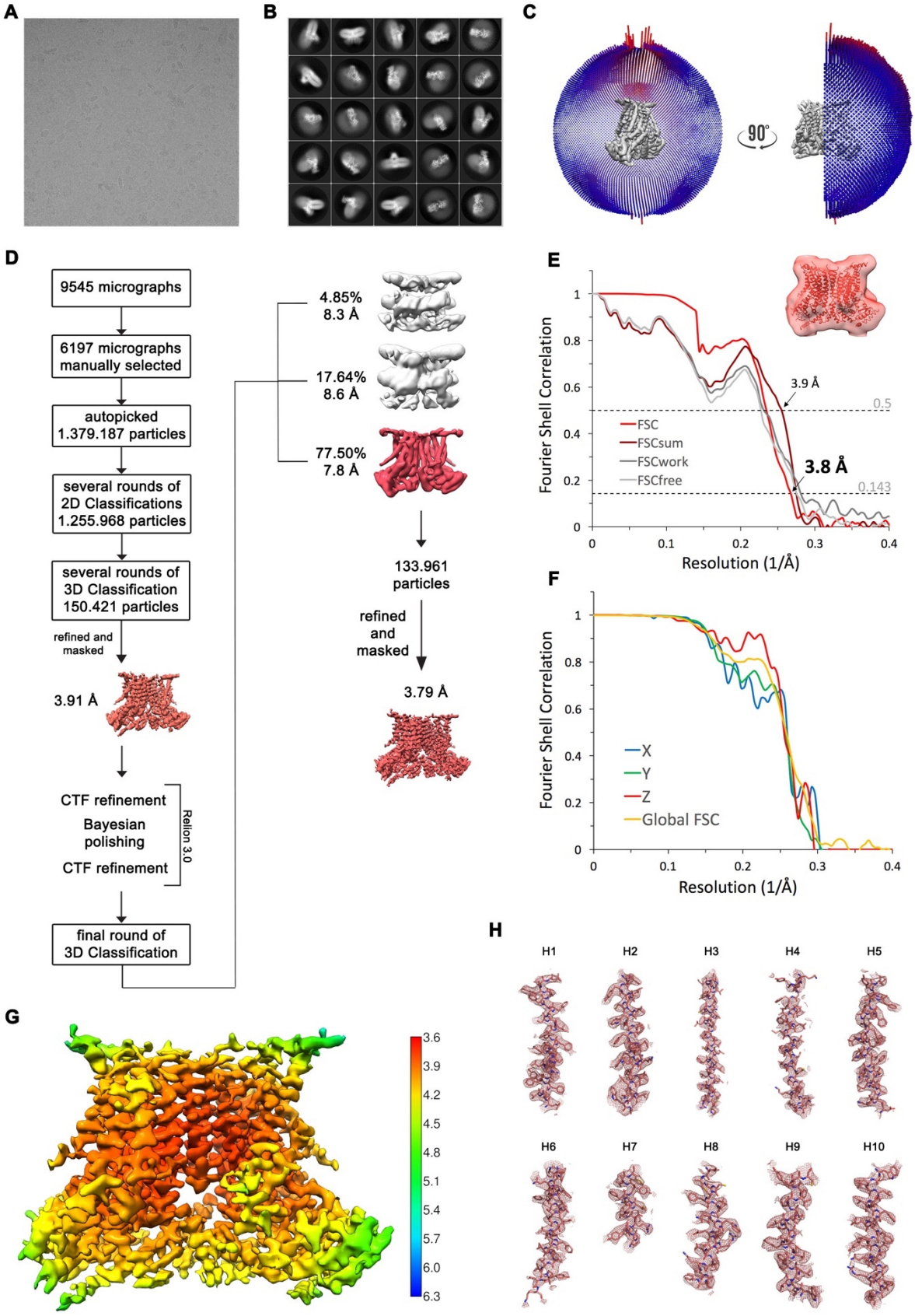
A
B
C
90°
D
9545 micrographs
6197 micrographs manually selected
autopicked 1.379.187 particles
several rounds of 2D Classifications 1.255.968 particles
several rounds of 3D Classification 150.421 particles
refined and masked
3.91 Å
CTF refinement
Bayesian polishing
CTF refinement
Relion 3.0
final round of 3D Classification
4.85% 8.3 Å
17.64% 8.6 Å
77.50% 7.8 Å
133.961 particles
refined and masked
3.79 Å
E
Fourier Shell Correlation
Resolution (1/Å)
FSC
FSCsum
FSCwork
FSCfree
3.9 Å
3.8 Å
0.5
0.143
F
X
Y
Z
Global FSC
G
3.6
3.9
4.2
4.5
4.8
5.1
5.4
5.7
6.0
6.3
H
H1
H2
H3
H4
H5
H6
H7
H8
H9
H10

Figure S4. Structure Determination of nhTMEM16 in the absence of Ca^{2+} in nanodiscs, Related to Figure 2

(A) Representative cryo- EM image and (B) 2D-class averages of vitrified nhTMEM16 in a Ca^{2+}-free state in lipid nanodiscs. (C) Angular distribution plot of particles included in the final C2-symmetric 3D reconstruction. The number of particles with their respective orientation is represented by length and color of the cylinders. (D) Image processing workflow. (E) FSC plot used for resolution estimation and model validation. The gold-standard FSC plot between two separately refined half-maps is shown in red and indicates a final resolution of 3.8 Å. FSC validation curves for FSCsum, FSCwork and FSCfree as described in Methods are shown in dark red, dark grey and light grey, respectively. A thumbnail of the mask used for FSC calculation overlaid on the atomic model is shown in the upper right corner and thresholds used for FSCsum of 0.5 and for FSC, FSCwork and FSCfree of 0.143 are shown as dashed lines. (F) Anisotropy estimation plot of the final map. The global FSC curve is represented in yellow. The directional FSCs along the x, y and z axis displayed in blue, green and red, respectively, are indicative for an isotropic dataset. (G) Final reconstruction map colored by local resolution as estimated by Relion, indicate regions of higher resolution. (H) Sections of the cryo-EM density of the map superimposed on the refined model. The model is shown as sticks and structural elements are labelled. The map was sharpened with a b-factor of –150 $Å^2$ and contoured at 5 σ.

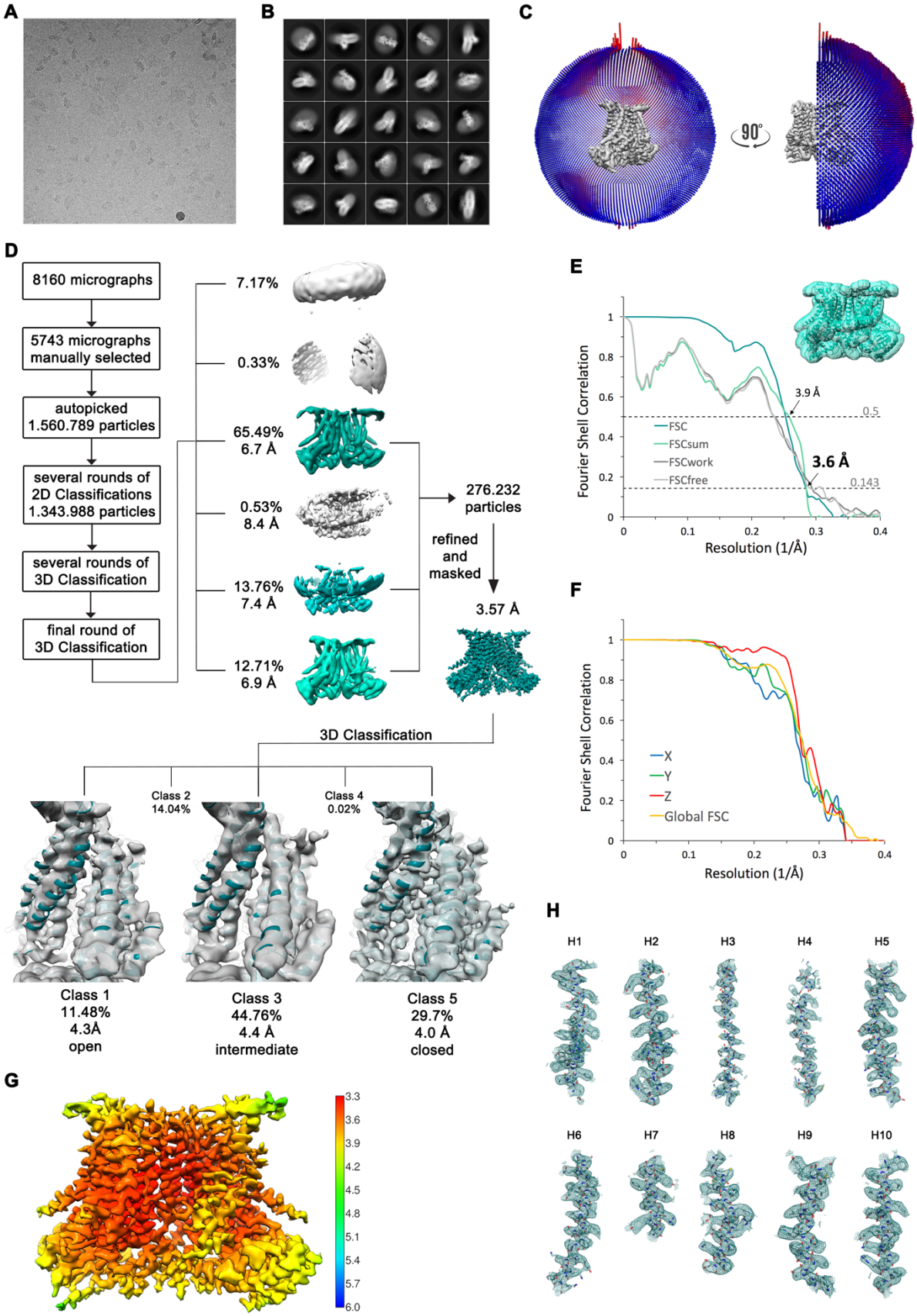
A
B
C
90°
D
8160 micrographs
5743 micrographs manually selected
autopicked 1.560.789 particles
several rounds of 2D Classifications 1.343.988 particles
several rounds of 3D Classification
final round of 3D Classification
7.17%
0.33%
65.49% 6.7 Å
0.53% 8.4 Å
13.76% 7.4 Å
12.71% 6.9 Å
276.232 particles
refined and masked
3.57 Å
3D Classification
Class 2 14.04%
Class 4 0.02%
Class 1 11.48% 4.3Å open
Class 3 44.76% 4.4 Å intermediate
Class 5 29.7% 4.0 Å closed
E
Fourier Shell Correlation
Resolution (1/Å)
FSC
FSCsum
FSCwork
FSCfree
3.9 Å
3.6 Å
0.5
0.143
F
Fourier Shell Correlation
Resolution (1/Å)
X
Y
Z
Global FSC
G
3.3
3.6
3.9
4.2
4.5
4.8
5.1
5.4
5.7
6.0
H
H1
H2
H3
H4
H5
H6
H7
H8
H9
H10

Figure S5. Structure Determination of nhTMEM16 in complex with Ca^{2+} in nanodiscs, Related to Figure 2

(A) Representative cryo- EM image and (B) 2D-class averages of vitrified nhTMEM16 in a Ca^{2+}-bound state in lipid nanodiscs. (C) Angular distribution plot of particles included in the final C2-symmetric 3D reconstruction. The number of particles with their respective orientation is represented by length and color of the cylinders. (D) Image processing workflow. The final map was subjected to a final round of 3D classification disclosing a conformational heterogeneity at the subunit cavity, with the main class resembling the intermediate state and two smaller classes resembling an open and close state of the subunit cavity. Close-views of the subunit cavity show the final model (dark green) superimposed on the cryo-EM maps of subclasses. (E) FSC plot used for resolution estimation and model validation. The gold-standard FSC plot between two separately refined half-maps is shown in dark green and indicates a final resolution of 3.6 Å. FSC validation curves for FSCsum, FSCwork and FSCfree as described in Methods are shown in light green, dark grey and light grey, respectively. A thumbnail of the mask used for FSC calculation overlaid on the atomic model is shown in the upper right corner and thresholds used for FSCsum of 0.5 and for FSC, FSCwork and FSCfree of 0.143 are shown as dashed lines. (F) Anisotropy estimation plot of the final map. The global FSC curve is represented in yellow. The directional FSCs along the x, y and z axis displayed in blue, green and red, respectively, are indicative for an isotropic dataset. (G) Final reconstruction map colored by local resolution as estimated by Relion, indicate regions of higher resolution. (H) Sections of the cryo-EM density of the map superimposed on the refined model. The model is shown as sticks and structural elements are labelled. The map was sharpened with a b-factor of –157 $Å^2$ and contoured at 5 σ.

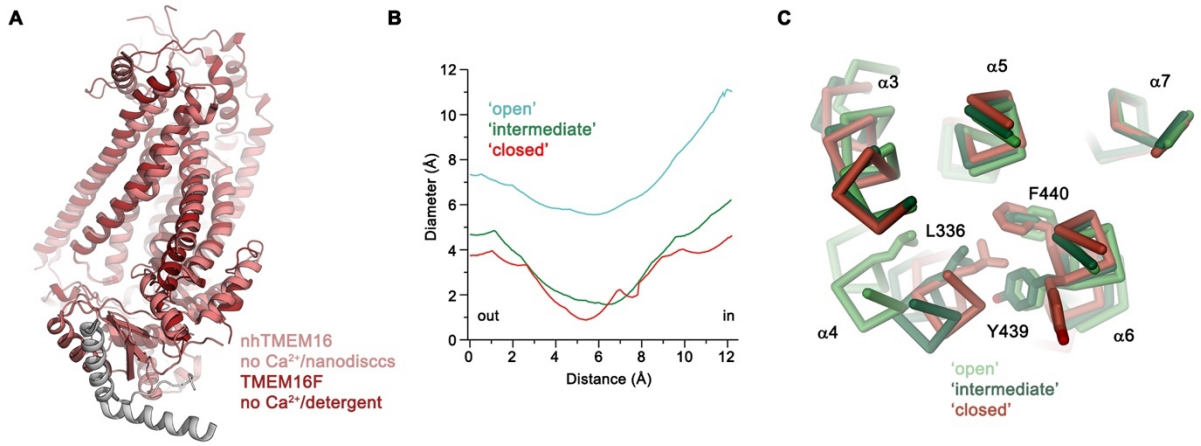

Figure S6. Features of nhTMEM16 structures, Related to Figure 4

(A) Ribbon representation of a superposition of the Ca^{2+}-free structure of nhTMEM16 in nanodiscs (light red and grey) and the Ca^{2+}-free structure of TMEM16F described in an accompanying study (dark red). (B) Pore diameter at the constriction of the subunit cavity in the three conformations calculated with HOLE (Smart et al., 1996). (C) View of the constriction of the 'subunit cavity' in three different conformations from the extracellular side. The protein is shown as Cα-trace with selected sidechains displayed as sticks.

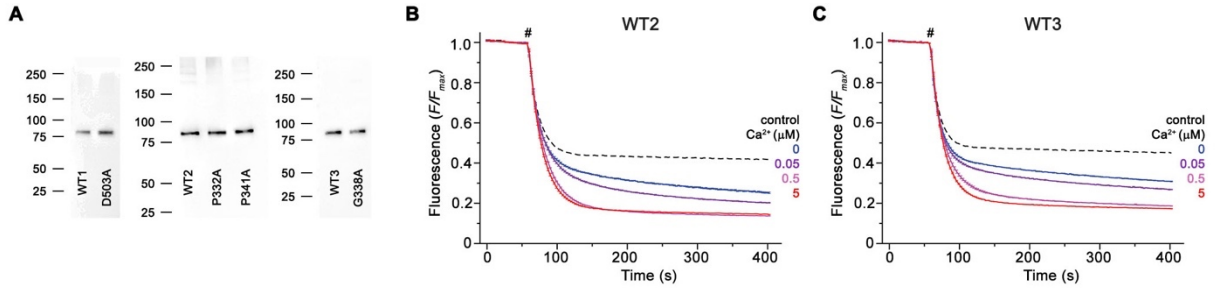

Figure S7. Reconstitution efficiency, Related to Figure 6

(A) Reconstitution efficiency of nhTMEM16 mutants compared to WT (WT1, WT2, WT3) reconstituted in the same batch of solubilized lipids. For analysis, equivalent amounts of liposomes were loaded on SDS-PAGE and detected with an anti-my antibody detecting a fusion tag on the protein. The positions of molecular weight markers (kDa) are indicated. See Figure 6B for traces

of WT1. (B) Ca^{2+}-dependence of scrambling activity of WT2 displayed for comparison in Figures 6D and 6F. (C) Ca^{2+}-dependence of scrambling activity of WT3 displayed for comparison in Figure 6E. Traces depict fluorescence decrease of tail-labeled NBD-PE lipids after addition of dithionite (#) at different Ca^{2+} concentrations. Data show averages of three technical replicates. Ca^{2+} concentrations (μM) are indicated.

Table S1. Cryo-EM data collection, refinement and validation statistics, Related to Figure 1 and 2

	nhTMEM16 DDM, +Ca^{2+} (EMDB …, PDB …)	nhTMEM16 DDM, -Ca^{2+} (EMDB …, PDB …)	nhTMEM16 2N2, +Ca^{2+} (EMDB …, PDB …)	nhTMEM16 2N2, -Ca^{2+} (EMDB …, PDB …)
Data collection and processing				
Microscope	Talos Arctica	Talos Arctica	Talos Arctica	Talos Arctica
Camera	K2 Summit + GIF	K2 Summit + GIF	K2 Summit + GIF	K2 Summit + GIF
Magnification	49,407	49,407	49,407	49,407
Voltage (kV)	200	200	200	200
Exposure time frame/total (s)	0.15/9	0.15/9	0.15/9	0.15/9
Number of frames per image	60	60	60	60
Electron exposure (e–/Å^2)	52	52	52	52
Defocus range (μm)	-0.5 to -2.0	-0.5 to -2.0	-0.5 to -2.0	-0.5 to -2.0
Pixel size (Å)	1.012	1.012	1.012	1.012
Box size (pixels)	220	256	240	240
Symmetry imposed	C2	C2	C2	C2
Initial particle images (no.)	251,693	435,660	1,560,789	1,379,187
Final particle images (no.)	120,086	214,170	276,232	133,961
Map resolution (Å)	3.6	4.0	3.6	3.8
0.143 FSC threshold				
Map resolution range (Å)	3.4-5.0	3.7-5.5	3.3-4.8	3.3-5.0
Refinement				
Initial model used	PDB 4WIS	PDB 4WIS	PDB 4WIS	PDB 4WIS
Model resolution (Å)				
FSC threshold				
Model resolution range (Å)	80-3.6	80-4	80-3.6	80-3.8
Map sharpening *B* factor (Å^2)	-126	-187	-157	-150
Model composition				
Nonhydrogen atoms	10972	10652	10814	10448
Protein residues	1362	1316	1336	1292
Ligands	4		4	
B factors (Å^2)				
Protein	18.58	9.47	12.17	15.33
Ligand	29.60	-	56.6	
R.m.s. deviations				
Bond lengths (Å)	0.007	0.007	0.010	0.011
Bond angles (°)	0.973	1.052	1.144	1.118
Validation				
MolProbity score	1.64	1.58	1.56	1.74
Clashscore	3.98	4.81	4.6	6.54
Poor rotamers (%)	1.55	0.53	0.87	1.08
Ramachandran plot				
Favored (%)	95.54	95.22	95.30	94.95
Allowed (%)	4.46	4.78	4.7	5.05
Disallowed (%)	0	0	0	0

Movie 1: Structure of nhTMEM16 in detergent in complex with Ca^{2+}, Related to Figure 1

Shown is the cryo-EM density map of nhTMEM16 obtained in complex with Ca^{2+} in detergent superimposed on the refined structure. For clarity, only a single subunit is shown (light green) with the cytosolic C-terminal helix of the adjacent subunit colored in grey. The cryo-EM map is depicted as surface, the model as light green sticks, and calcium ions as orange spheres.

Movie 2: Structure of nhTMEM16 in detergent in absence with Ca^{2+}, Related to Figure 1

Shown is the cryo-EM density map of nhTMEM16 obtained in absence of Ca^{2+} in detergent superimposed on the refined structure. For clarity, only a single subunit is shown (coral) with the cytosolic C-terminal helix of the adjacent subunit colored in grey. The cryo-EM map is depicted as surface and the model as coral sticks.

Movie 3: Structure of nhTMEM16 in nanodiscs in absence with Ca^{2+}, Related to Figure 2

Shown is the cryo-EM density map of nhTMEM16 obtained in complex with Ca^{2+} in lipid nanodiscs superimposed on the refined structure. For clarity, only a single subunit is shown (red) with the cytosolic C-terminal helix of the adjacent subunit colored in grey. The cryo-EM map is depicted as surface and the model as red sticks.

Movie 4: Structure of nhTMEM16 in nanodiscs in complex with Ca^{2+}, Related to Figure 2

Shown is the cryo-EM density map of nhTMEM16 obtained in complex with Ca^{2+} in lipid nanodiscs superimposed on the refined structure. For clarity, only a single subunit is shown (green) with the cytosolic C-terminal helix of the adjacent subunit colored in grey. The cryo-EM map is depicted as surface, the model as green sticks, and calcium ions as orange spheres.

Movie 5: Conformational transitions, Related to Figure 3

Shown is a morph between distinct conformational states obtained for nhTMEM16, namely: the open state obtained for nhTMEM16 in detergent in complex with Ca^{2+}, the intermediate state obtained for nhTMEM16 in lipid nanodiscs in complex with Ca^{2+} and the closed state obtained for nhTMEM16 in lipid nanodiscs in absence of Ca^{2+}. For clarity only transmembrane α-helices 3 and 8 are shown and at the beginning Ca^{2+} ions are depicted as orange spheres.

Movie 6: Micelle and lipid distortion, Related to Figure 5

Shown are the cryo-EM density maps of nhTMEM16 obtained in detergent in complex with Ca^{2+} (upper left corner, light green and grey), in detergent in absence of Ca^{2+} (upper right corner, coral and grey), in lipid nanodiscs in complex with Ca^{2+} (lower left corner, green and grey) and in lipid nanodiscs in absence of Ca^{2+} (lower right corner, red and grey). The surrounding environment corresponding to the detergent micelle (upper panels) or the lipid nanodiscs (lower panels) are colored respectively, while the rest of the protein is shown in grey. Transmembrane α-helices 4 and 6 are labeled at the end, indicating the position of the subunit cavity.